nature communications

Article

https://doi.org/10.1038/s41467-025-58557-0

Junctional force patterning drives both positional order and planar polarity in the auditory epithelia

Received: 28 February 2024

Accepted: 19 March 2025

Published online: 26 April 2025

Check for updates

Anubhav Prakash[1,4], Julian Weninger[2,4], Nishant Singh[1,3], Sukanya Raman[1], Madan Rao[1], Karsten Kruse[2,5] ✉ & Raj K. Ladher[1,5] ✉

Tissue function depends on the precise organisation of the constituent cells. In the cochlea, the fidelity of hearing depends on mechanosensory hair cells being consistently surrounded by supporting cells. In addition to this positional order, auditory sensitivity depends crucially on planar cell polarity. This is characterised by the alignment of the orientation of eccentrically placed hair bundles on each hair cell. These two levels of order emerge simultaneously despite the cellular fluxes that occur during cochlear development. However, the link between tissue-scale cellular rearrangements and intrinsic cellular mechanisms remains unknown. By combining experimental and theoretical approaches, we find a precise force patterning underpinning positional order and planar cell polarity. This occurs through the modulation of the levels and phospho-type of the regulatory light chain of non-muscle myosin II at specific cell-cell junctions of the auditory epithelium. We propose that the control of junctional mechanics is vital for the organisation of multi-cell-type epithelia.

The reception and transduction of auditory information by the cochlea of the inner ear requires exquisite levels of organisation of its constituent cells: hair cells (HCs) and supporting cells (SCs). Each HC is intrinsically polar as the mechanosensory hair bundle, consisting of kinocilium and stereocilia, is eccentrically positioned on the HC apex. This intrinsic polarity aligns across the tissue axis such that the epithelium displays a tissue-wide planar polarity, ensuring a concerted and sensitive response to sound[1]. HCs themselves are always surrounded by SCs, a spatial organisation that is necessary to maintain ionic homoeostasis during transduction. As development proceeds, the spatial organisation is further refined, with HC becoming positionally ordered within a regular mosaic of SC. HC and SC differentiation occurs while the auditory epithelium undergoes extension through cell intercalation via junctional remodelling[2,3]. Even amid these rearrangements, both spatial organisation and planar polarity emerge[4].

Mechanical forces are known to generate planar polarity in simple epithelia with single cell type. In the Drosophila wing disk, which comprises a single anisotropic cell type, planar polarity ordering results from the mechanical forces that direct cell flows during development[5,6]. However, in epithelia that are made up of more than one cell type, the different cell types must be coupled so that juxtacellular events can be coordinated across the tissue. In simulations of the developing mouse cochlea, shear forces from differential cell flows can generate spatial organisation[7]. However, these rearrangements cannot explain the development of planar polarity and thus do not provide insights into its link to spatial organisation. Experimentally, disrupting heterophilic adhesion between HC and SC perturbs both planar polarity and spatial organisation[8,9], suggesting a mechanistic link. However, how cell patterns and cell rearrangements can be coordinated to generate both positional and orientational ordering is not known.

[1]National Centre for Biological Sciences, Tata Institute for Fundamentals Research, GKVK PO, Bangalore, India. [2]Departments of Biochemistry and Theoretical Physics, University of Geneva, Geneva, Switzerland. [3]The University of Trans-Disciplinary Health Sciences and Technology, Yelahanka, Bangalore, India. [4]These authors contributed equally: Anubhav Prakash, Julian Weninger. [5]These authors jointly supervised this work: Karsten Kruse, Raj K. Ladher. ✉e-mail: Karsten.Kruse@unige.ch; rajladher@ncbs.res.in

Using the chick auditory epithelium (also known as the basilar papilla), we show that positional order and planar polarity develop from mechanical heterogeneities generated by the type and amount of phosphorylation on the regulatory light chain (RLC) of myosin-II. The positional ordering of HC and SC, relies on cell-specific developmental programmes that restrict di-phosphorylated RLC to junctions between SC, while the mono-phosphorylated form is found on HC-SC junctions. The amount of RLC phosphotype is further tuned through cues provided by core PCP molecules, defining the tissue axis, and the HC-intrinsic polarity pathway. These two layers of regulation lead to different types of contractility on different types of junctions, resulting in a tissue-wide orientational order. Using experiments and theory, we show that these nested asymmetries tune the mechanical activity of individual junctions to establish tissue-wide force patterns that result in both positional ordering and planar polarity alignment.

Results

Positional order and planar polarity are generated simultaneously in the auditory epithelium

The avian auditory epithelium, the basilar papilla (BP), is a sickle-shaped epithelium contiguous with the rest of the inner ear (Fig. 1A; Supplementary Fig. 1A). We asked when HC intrinsic polarity develops and whether it is already globally aligned when it is first apparent. BPs from embryos between embryonic days (E) 8 and E14 were stained with phalloidin to mark junctional actin, allowing us to segment cell boundaries (Fig. 1B), with hair cell antigen (HCA) to identify HCs, and for the intraflagellar transport component IFT88 to obtain the position of the hair cell kinocilium (Fig. 1B; Supplementary Fig. 1B–D)[10,11]. We used this to measure HC intrinsic polarity in different regions of the BP (Supplementary Fig. 1A), defining a polarity vector as the vector pointing from the geometric centre of the cell apical surface to the kinocilium base, with a correction for cell elongation (Supplementary Fig. S1E, F). The vector was normalised, with 1 being a kinocilium on the cell boundary and an angle to the P-D axis. At E8, we found that the HCs were not polarised, with the kinocilium located close to the geometric centre of the HC (magnitude 0.09 at position 25I and 0.07 at position 75I, Fig. 1C). By E10, the kinocilium had deflected eccentrically (magnitude 0.31 at 25I and 0.20 at 75I), providing HCs an intrinsic polarity. Crucially, HC polarity was only locally aligned, with kinocilia of HCs on the proximal side of the BP deflected proximally (223° ± 42°, circular mean and circular standard deviation) and kinocilia of distal HCs deflected distally (356° ± 55°) (Fig. 1A–C; Supplementary Fig. 1G). By E12, the circular standard deviation (c.s.d.) of HC polarity across the entire BP had dramatically reduced, and all kinocilia were oriented towards the inferior edge of the BP with a mean angle of 279° ± 37° and 274° ± 34°, at 25I and 75I respectively, indicative of an increase in the alignment of HC polarity to tissue axis. By E14, planar polarity was further refined, with a reduction in c.s.d to 15° and 16°, respectively (Fig. 1C). These data suggested that the generation of polarity in the BP is a biphasic process; a local polarity generated at E10 is transformed to a globally aligned planar polarity across the entire epithelium by E12, which further refines by E14.

Previous studies have described cell rearrangements between E10 and E12[12]. To investigate a possible correlation between polarity and geometry across the tissue, we determined neighbour numbers for both HCs and SCs (Fig. 1D). At all stages and all positions on the BP, contacts between two HCs were rare, such that HCs were surrounded only by SCs. At 25I, between E8 to E12, the mean number of SCs each HC contacts, termed HC neighbour number, increased from 5 to 8. A SC can neighbour both HCs and other SCs. As the total number of SC neighbours decreased between E8 and E12 from 7 to 5, the mean number of HCs they contacted increased from 1 to 2 (Fig. 1B, D). These trends are mirrored across the entire epithelium (Supplementary Figs. 1G, 2A, B; Supplementary Table 1). The spatial organisation of HCs can be described by a (corrected) hexatic order parameter ψ_6^*, which quantifies the angular order of proximate HCs and is 1 for a perfect hexagonal lattice (Supplementary Fig. 2C). We use both the neighbour number of HCs and SCs along with hexatic order parameter to describe the positional order in BP. During development, the hexatic order increased from 0.2 at E8 to 0.65 at E14 (Supplementary Fig. 2D). When studied with the development of planar polarity, we found that c.s.d of HC polarity negatively correlated with the hexatic order parameter (Fig. 1E). This suggests a temporal coupling between positional order and planar polarity.

To ask if positional order and planar polarity were mechanistically coupled, we took a genetic approach to disrupt positional order by perturbing the ratio of HCs to SCs. The transcription factor Atoh1 is necessary for HC development[13,14]. We hypothesised that by knocking down Atoh1 we could reduce the number of HCs. Using electroporation, we introduced gRNA constructs targeting the chick Atoh1 gene and an eGFP plasmid into the otic vesicle at E3.5 (Supplementary Fig. 3A). Embryos were cultured to E11, at which point the BP was dissected. Electroporation is mosaic, and in Atoh1 deleted patches, marked by eGFP expression, HC number was reduced (Supplementary Fig. 3B, C). The HCs in these patches made comparable contacts as those in controls (Supplementary Fig. 3D, E, Supplementary Table 2), however hexatic order was significantly reduced (0.26 compared to 0.48 in controls). SCs from these patches showed higher variance in their neighbour numbers, further indicating a decrease in positional order (Supplementary Fig. 3D, E). Importantly, in these patches, the polarity for the HCs was not aligned (c.s.d. of 87°), when compared to controls (c.s.d. of 21°) (Supplementary Fig. 3F). These data further support that the acquisition of positional order is coupled to the alignment of HC polarity throughout the BP and that a common underlying mechanism likely drives both.

Systematic Mechanical Heterogeneities drive Positional Ordering

To understand the mechanisms of positional ordering of HC and SC, we investigated the development of these neighbourhoods. From E8 to E14, the apical surface area of HCs increased 10-fold from $5.9 \pm 1.6\ \mu m^2$ to $69 \pm 13\ \mu m^2$ while that of SCs decreased 2-fold from $9.9 \pm 3.6\ \mu m^2$ to $5.2 \pm 2.1\ \mu m^2$ (Fig. 2A; Supplementary Fig. 4A). In most epithelia, the average cell area increases linearly with the neighbour number n, formalised by the empirical Lewis law[15]. In the BP, SCs show this linear relationship (Supplementary Fig. 4B). In contrast, at any developmental stage between E8 and E14, HC area shows almost no dependence on neighbour number (Supplementary Fig. 4B). Therefore, we sought to better understand the geometric difference between HCs and SCs. We started with E10, where HC and SC apical surface areas are similar, with 7.3 ± 1.8 and $8.7 \pm 3.4\ \mu m^2$, respectively. However, at these stages, we found that the HC neighbour number (4–5 neighbours) was significantly different from that of SCs (6–7 neighbours, Fig. 2B). This deviation, together with a mathematical relation for planar graphs based on Euler's formula indicate that the BP comprises of two geometrically different cell types. As proliferation and differentiation are rare after E9 (Supplementary Fig. 4C–E)[16], we suggest that mechanical differences between HCs and SCs could explain these observed differences at E10.

Tissue mechanics is regulated by the actomyosin complex, with non-muscle myosin 2 (NMII) as the motor component. NMII is a hetero-hexameric holoenzyme with two heavy chains carrying the motor activity (MHC), two essential light chains, and two regulatory chains (RLC)[17]. NMII activity depends on either mono- (p-RLC) or di- (pp-RLC) phosphorylation[18]. These forms determine the ATPase activity of NMII and in this way, the binding kinetics of NMII to actin filaments[19,20]. We, therefore, mapped the active forms of NMII during the generation of positional order. Immunostaining of the BP revealed p-RLC on both HC-SC and SC-SC junctions (Fig. 2C). In contrast, pp-RLC was only

https://doi.org/10.1038/s41467-025-58557-0

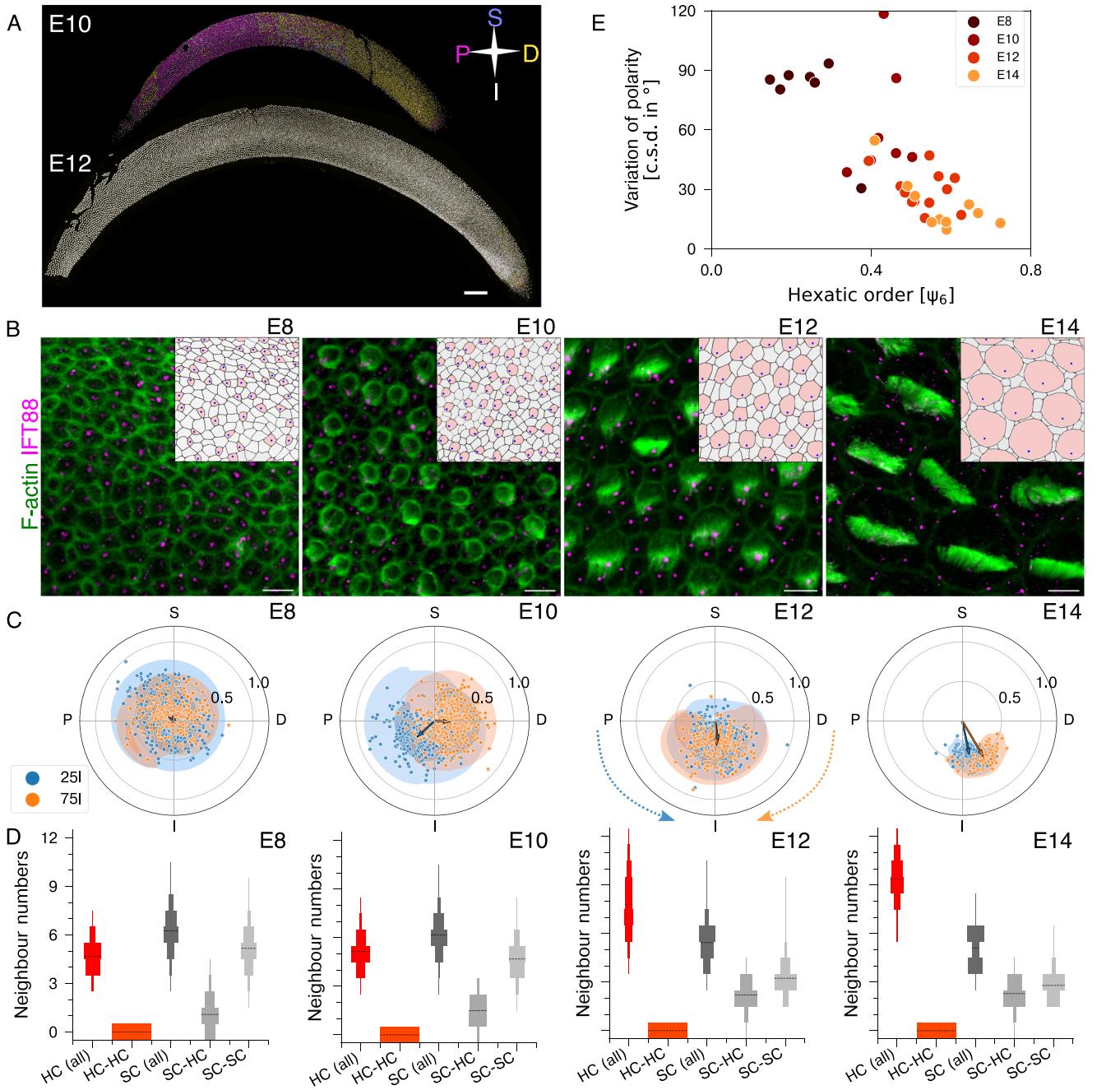

Fig. 1 | Planar polarity and positional ordering develop concomitantly in the chick Basilar Papilla (BP). A BP stained with hair cell antigen (HCA) at Embryonic day (E)10 and E12 colour coded for proximally (P, magenta), distally (D, yellow), superiorly (S, blue), and inferiorly (I, white) deflected kinocilia. $N = 3$ embryos. Scale bar: 100 µm. **B** Proximal inferior (25I) part of BP stained for Phalloidin (green) and IFT88 (magenta) to mark junctions and kinocilia respectively (In inset, junctions in black, Hair cells in pink, supporting cell in grey, kinocilia in blue) at E8, E10, E12, and E14. Scale bar: 5µm. $N \geq 3$, Supplementary Table 1. **C** Positions of HC kinocilia in polar coordinates from the proximal (25I, blue) and distal (75I, orange) part of BP at E8, E10, E12, and E14. Positions are corrected for cell elongation (Methods). Arrows indicate the respective mean polarity for the proximal (blue) and distal (orange) parts. $N = 328/293$ (25I/75I, E8), 225/363 (E10), 370/255 (E12), 117/91 (E14). **D** Distribution of the number of neighbours for HCs (red) and SCs (grey) at 25I for E8, E10, E12, and E14. Neighbourhoods are subdivided further into HC-HC (orange, 0 during normal development), SC-HC, and SC-SC contacts (greys). Histogram widths indicate probability distribution. Dashed lines indicate mean. $N = 425/1752$ (HC/SC, E8), 601/2003 (E10), 623/2255 (E12), 180/420 (E14). **E** The circular standard deviation (c.s.d.) of HC polarity over the hexatic order ψ_6 for stages E8–E14. See methods. Image orientation: D – right, S – up. Experimental values in Supplementary Table 1.

observed at SC-SC junctions (Fig. 2D). Previous studies have associated pp-RLC with increased stability and filament assembly[18] as well as stress fibre tension[21]. Using a live imaging approach, we asked whether pp-RLC leads to mechanical differences in the SC-SC junctions. BP explants were stained with SiR-Actin, marking junctional actin and nascent stereocilia to highlight junctions and hair bundles. We imaged these explants for 8 h (Supplementary Movie 1), measuring the length fluctuations of HC-SC and SC-SC junctions. We found that length fluctuations of SC-SC junctions were significantly lower than those of HC-SC junctions (Fig. 2E).

Fluctuations in the length of junctions are due to the stochastic turnover of NMII at the junction. Due to decreased ATPase activity, NMII carrying p-RLC has a higher off-rate from actin filaments, thus generating less force than NMII carrying pp-RLC[22,23]. A theoretical

https://doi.org/10.1038/s41467-025-58557-0

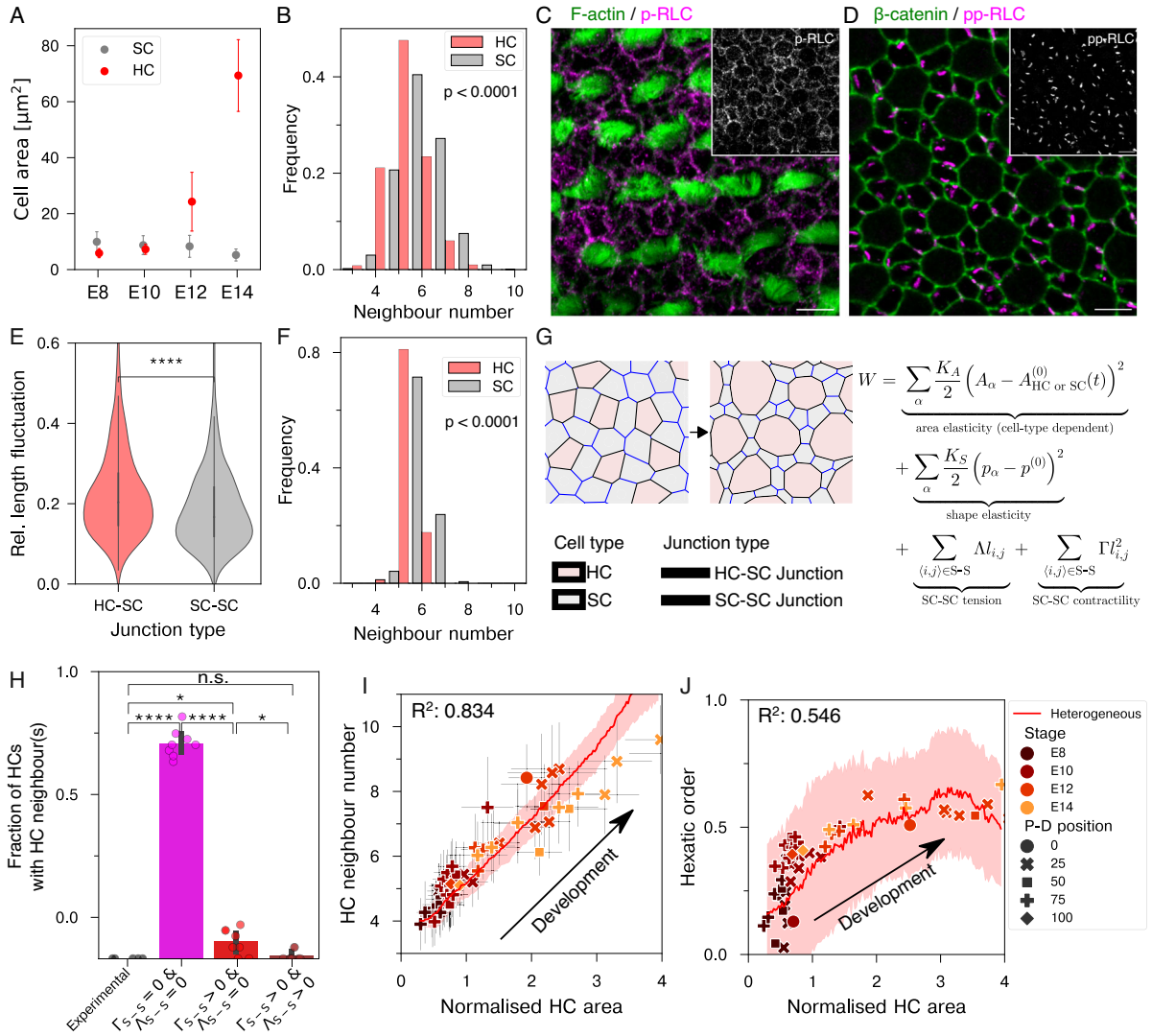

Fig. 2 | Mechanical heterogeneity of junctions drives positional order of BP. **A** Apical surface area of HCs (red) and SCs (grey) at the 25I position at E8 to E14, bars represent std dev. N = (no of embryos: no of HC/no of SC); E8 (4: 332/985), E10 (5: 601/2003), E12 (6: 623/2255), E14 (3: 180/799). **B** Comparison of distribution of neighbour numbers of HCs (red) and SCs (grey) at equal surface area (25I, E10) determined experimentally. The average number of neighbours for HC (5.16) significantly differs from that of SC (6.18). **C** E12 BP stained for F-actin (green) and monophosphorylated, p-RLC of Non-Muscle Myosin II (magenta and inset). $N = 6$ embryos. **D** E12 BP stained for β-catenin (green) and di-phosphorylated pp-RLC of Non-Muscle Myosin II (magenta and inset). $N = 6$ embryos. **E** Relative length fluctuation of HC-SC and SC-SC junctions. $N = 474/479$ (HC-SC/SC-SC). **F** Comparison of distribution of neighbour numbers of HC (red) and SC (grey) at equal surface area determined in a vertex model using increased contractility on SC-SC junctions. The average number of neighbours for HC (5.16) significantly differs from that of SC (6.21). **G** Schematic representation of the 2D-vertex model with heterogeneous junctional contractility and increasing area of HCs used to describe the BP development. **H** Fraction of HC-HC contacts at 25I position at E10 determined experimentally ($N = 5$) and using theory with homogenous junctional mechanics (magenta), with only additional contractility on SC-SC junction (red) and with both additional contractility and line-tension on SC-SC junction (brown). Bars indicate mean and error bars indicate std. dev. **I** Number of HC neighbours increase with normalised HC area in the BP. Data points represent individual images from positions along the P-D axis of BP, Red line shows the theoretical observation when changing target HC area with additional contractility on SC-SC junctions. **J** Hexatic order increases with normalised HC area in BP. Data points represent individual images from positions along the P-D axis of BP. Crosses indicate sample std. dev. Red line shows the theoretical observation when changing target HC area with additional contractility on SC-SC junctions. For **I** and **J**, $N = 13$(E8), 22(E10), 14(E12), 12(E14). Crosses and shaded areas indicate sample std. dev. n.s.: $p >= 0.05$, *$p < 0.05$, ****$p < 0.0001$: Unpaired Two-tailed T-test. Scale bar: 5μm. Image orientation: D – right, S – up. Parameter values for (**F**, **H**) in Supplementary Table 6 (best fit), for (**I**, **J**) in Supplementary Table 7.

analysis of these binding dynamics shows that pp-RLC enriched junctions (SC-SC) are under more tension than junctions richer in p-RLC (HC-SC) and fluctuate less in length (Methods; Supplementary Fig. 4F) which suggests that SC-SC junctions are more contractile than HC-SC junctions.

To understand how differential contractility could contribute to positional ordering, we used 2D vertex modelling. This has provided insights into the morphogenesis of epithelia that are made of single-cell types. These include the growth of the Drosophila wing[5,24], the closure of the neural tube[25], in wound healing[26] and the patterning of the zebrafish retina[27]. We adapted this framework to an explicit two-cell-type system to ask whether the differential junctional contractility of HC-SC and SC-SC junctions is sufficient to shape HC and SC neighbourhoods. Here, the apical surface of a tissue is represented by a polygonal meshwork, where the edges of the meshwork represent the interfaces between neighbouring cells. The configuration of the meshwork is chosen such that it minimises the work function W. This work function depends on the cell areas, A_α, normalised cell perimeters (termed cell shape indices, p_α), and junctional lengths, $l_{i,j}$. Most generically, for the two-cell-type tissue, this

can be written as

$$W = \underbrace{\underbrace{\sum_\alpha \frac{K_A}{2}\left(\frac{A_\alpha}{A_\alpha^{(0)}}-1\right)^2}_{\text{area elasticity}} + \underbrace{\sum_\alpha \frac{K_S}{2}\left(p_\alpha - p_\alpha^{(0)}\right)^2}_{\text{shape elasticity}}}_{cell-type\ dependent} + \underbrace{\underbrace{\sum_{\langle i,j\rangle}\Lambda_{i,j}l_{ij}}_{\text{line tension}} + \underbrace{\sum_{\langle i,j\rangle}\Gamma_{i,j}l_{ij}^2}_{\text{junctional contractility}}}_{junction-type\ dependent}. \quad (1)$$

Here, α indexes cells and {i,j} edges connecting the vertices i and j. Deviations from a target area $A_\alpha^{(0)}$ and shape index $p_\alpha^{(0)}$ are penalised by the elastic constants K_A and K_S. Interfacial tension and junctional contractility are characterised by the parameters $\Lambda_{i,j}$ and $\Gamma_{i,j}$, respectively. We initiated our simulations with a random distribution of polygonal cells that had the same parameter values. We then randomly assigned a fraction, ρ, of cells to be HCs, with the rest being SCs. From our observations in the E10 BP, where the surface areas of HC and SC are similar, we considered uniform target areas $A_\alpha^{(0)} = A_H^{(0)} = A_S^{(0)} = 1$. We next introduced junctional mechanical parameters $\Lambda_{i,j}$ and $\Gamma_{i,j}$ that depend on the specific cell-cell interface types, namely those between HC-HC, HC-SC, and SC-SC.

To test whether the higher contractility on SC-SC junctions causes geometrical differences between HCs and SCs, we simulated two different E10 BPs, one in which there is no difference in contractility between the different interfaces ($\Gamma_{S,S} = \Gamma_{H,S}$: homogenous vertex model) and the other where SC-SC junctions are more contractile ($\Gamma_{S,S} > \Gamma_{H,S}$: heterogeneous vertex model; Methods). In the homogenous vertex model, HC neighbour numbers are similar to SC neighbour numbers (Supplementary Fig. 4G), and we observed frequent HC-HC contacts (80% of all HC contact another HC) which are never observed experimentally. In the heterogeneous vertex model, the number of HC and SC neighbours in the simulation showed a good quantitative fit with those observed empirically (Fig. 2F, G; Supplementary Fig. 4H–J). Moreover, the frequency of HC-HC contacts was reduced (10% of all HC contact another HC, Fig. 2H). Indeed, we were able to resolve HC-HC contacts in the homogenous vertex model, by SC-SC contractility after these aberrant contacts had been made. We hypothesised that as well as heterogeneous contractility, heterogeneous line tension may also reduce HC-HC contacts. By increasing SC-SC tension in our heterogeneous vertex model, we were able to further suppress HC-HC contacts (<2%; Supplementary Fig. 4G–I; Supplementary Movie 2). Repeating our simulations with heterogeneous line tension alone, we were able to reduce HC-HC contacts; however, in contrast to experimental observation (Supplementary Fig. 4G-I), the neighbour number of HCs and SCs remained similar. Together, these results show that heterogeneous junctional contractility is sufficient for generating positional order at E10.

To understand the positional ordering of the BP beyond E10, we next incorporated the increase in HC surface area into our model with increased SC-SC contractility and line tension (Fig. 2G). HC surface area increases through partial extrusion as the HC detaches from the basal lamina from E10 (Supplementary Fig. 5A–C). We incorporated the relative change of HC and SC area as a stepwise and quasi-static change of the target area parameter $A_\alpha^{(0)}$, keeping the total tissue size constant in our simulations (Supplementary Fig. 5D; Supplementary Movie 3). We observed a linear relation between average HC neighbour number and average HC area in our simulations, mirroring our experimental data (Fig. 2I; Supplementary Fig. 5E–G). With increasing HC area, we also observed a significant increase in hexatic order in our vertex model simulations, in agreement with our experimental observations (Fig. 2J). The emergence of hexatic order in auditory epithelia was previously described in the mouse[7]. These authors evoked long-range repulsion between, and external forcing of, HCs. In contrast, our experimental and theoretical results reveal pp-RLC contractility on SC-SC junctions and differential increases in apical surface area are sufficient to drive positional order.

To experimentally test the requirement of junctional heterogeneity for proper positional order, we used an organ culture to grow E10 BP in the presence of small molecule inhibitors of the RLC phosphorylation regulators, Rho-Associated Kinase (ROCK) and Myosin-Light Chain Kinase (MLCK)[28,29]. ROCK expression is found in HC and SC (Fig. S6A), however the expression of MLCK was only found in SCs (Fig. 3A). We treated E10 explanted chick BP with pharmacological inhibitors of ROCK (Y-27632) or MLCK (ML-7) for 4 h. ROCK inhibition repressed both p-RLC and pp-RLC (Supplementary Fig. 6B, C). In contrast, ML-7 inhibition resulted in the abrogation of pp-RLC but not p-RLC (Fig. 3B, C). Using F-actin and IFT88 staining, we assessed BP morphology in the ROCK and MLCK-inhibited explants. In both cases, we observed frequent HC-HC contacts, and a decrease in HC hexatic order for ROCK (0.44 ± 0.02 to 0.31 ± 0.01) and MLCK (0.47 ± 0.03 to 0.36 ± 0.04) inhibition, reflecting a reduction in positional ordering (Fig. 3D, E; Supplementary Fig. 6D, F, G; Supplementary Table 2). In ML-7 inhibited samples, HC neighbour number decreased and SC neighbour number increased (Fig. 3D, E). Interestingly, in both ROCK and MLCK inhibition, we observed an increase in the c.s.d of HC kinocilia, indicating a reduction in planar polarity (Fig. 3F; Supplementary Fig. 6H; Supplementary Table 2).

Our model predicted a resolution of the HC-HC contacts by introducing SC-SC contractility (Supplementary Fig. 6E; Supplementary Movie 4). Therefore, we restored heterogeneous contractility by washing out the inhibitor. Here, we incubated E10 BP explants for 4 h in either ML-7 or Y-27632 followed by two rinses in culture media and then continued culture for another 12 h (Supplementary Fig. 6D). We observed a restoration in HC and SC neighbour numbers, and hexatic order, as well as a resolution of HC-HC contacts in both ROCK and ML7 inhibited explants (Fig. 3G–I; Supplementary Fig. 6I, J, L-N). Although Y-27632 wash-off did not restore alignment of HC polarity, we found that by removing ML-7, the c.s.d of HC polarity was reduced, suggesting an increase in alignment of HC polarity (Fig. 3J; Supplementary Fig. 6K; Supplementary Table 2).

To ask whether ML-7 affected junctional contractility, we live-imaged SiR-actin-stained BP in the presence of ML-7 (Supplementary Movie 5). We found that the junctional length fluctuations were significantly increased on SC-SC junctions when compared to control ($p < 0.0001$), and similar to HC-SC junctions of control ($p > 0.3$) and ML-7 treated samples ($p > 0.2$) (Fig. 3K). This suggests that pp-RLC on SC-SC junctions regulates differential contractility.

Taken together, our results from both theory and experiments suggest that pp-RLC-driven higher contractility on SC-SC junctions, together with an increase in apical surface area, are drivers of positional order. Furthermore, the restoration of hexatic order, and the reduction of polarity variance in the ML-7 rescued explants strongly suggest that mechanical heterogeneity can couple HC positional order to HC orientational order.

Tuning of RLC phosphorylation drives Planar Polarity

We sought to investigate the putative mechanical coupling between the positional order and planar polarity. Previous studies in the mouse have shown that the apical polarity of a HC, indicated by the position of the kinocilium, is governed by the activity of the LGN-Gαi complex[30–32]. In the chick BP, both LGN and Gαi are localised to HC-SC junctions closest to the kinocilium (Supplementary Fig. 7A, B). In worms, this complex regulates myosin flows through RLC phosphorylation[33]. We therefore hypothesised that the LGN-Gαi complex, which dictates HC intrinsic polarity, also dictates HC-SC junctional contractility, establishing mechanical asymmetries around HCs.

https://doi.org/10.1038/s41467-025-58557-0

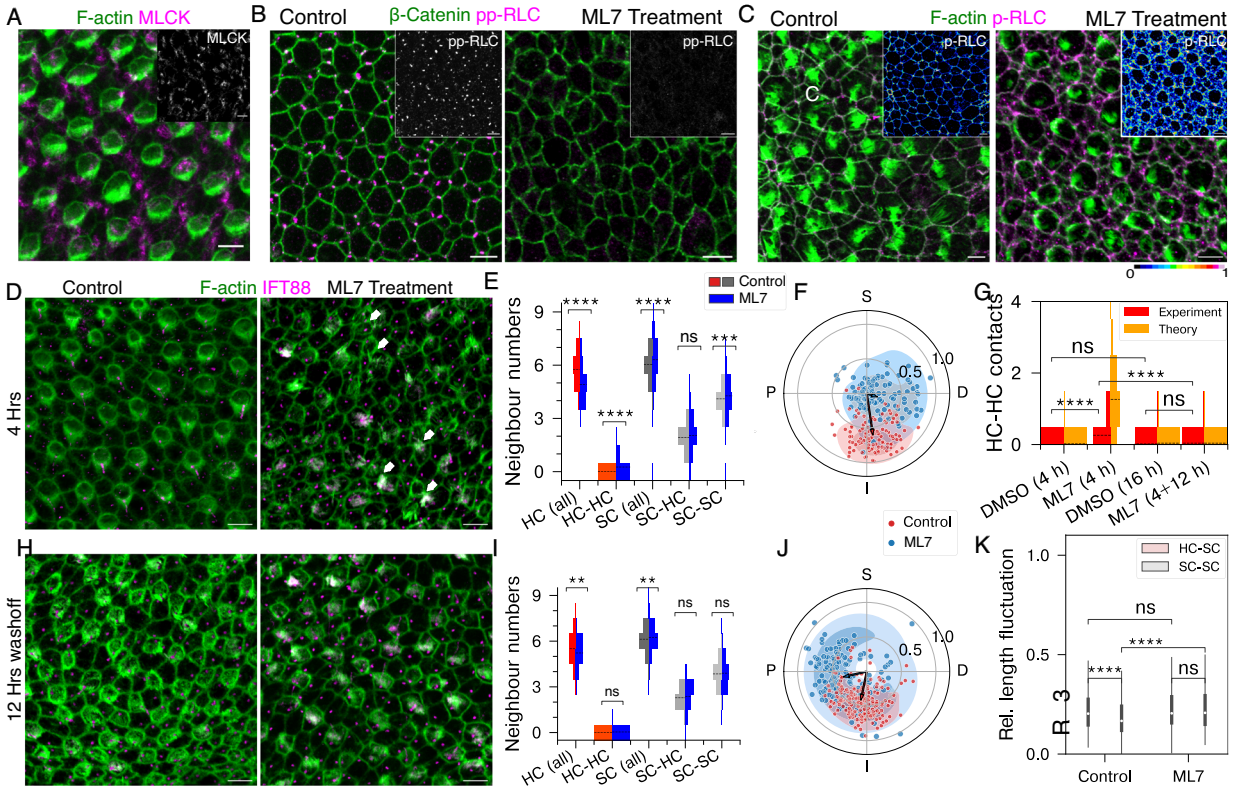

Fig. 3 | pp-RLC leads to higher contractility of SC-SC junction and is indispensable for planar polarity and positional order. A E12 BP stained for F-actin (green) and Myosin Light Chain Kinase (magenta and inset). $N = 5$ embryos. B. Expression of β-catenin (green) and pp-RLC (magenta, inset) in DMSO and ML7-treated E10 explants, respectively. $N = 6$ embryos. **C** Expression of F-actin (green) and p-RLC (magenta, inset) in DMSO and ML7 treated E10 explants, respectively. $N = 6$ embryos. **D** BP stained for F-actin (green) and IFT88 (magenta) treated with DMSO (control) or 25 μM ML7 for 4 h. Arrows indicate HC-HC contacts. $N = 6$ embryos. **E** Distribution of neighbour numbers for control BP (left split) and BP treated with ML7 for 4 h (right split). Dotted line represents mean. **F** Positions of HC kinocilia in polar coordinates from BP treated with DMSO (red) and ML7 (blue) for 4 h, respectively. Arrows represent mean orientation for DMSO (red) and ML7-treated (blue) explants. $N = 112/115$ (DMSO/ML7). **G** Comparison of distribution of HC-HC contacts between experiment (red) and theory (yellow) in the inhibition of junctional heterogeneity and its rescue. $N = 3$ embryos. **H** BP stained for F-actin (green) and IFT88 (magenta) treated with DMSO (control) or 25 μM ML7 for 4 h followed by rescue for 12 h. $N = 3$ embryos. **I** Distribution of neighbour numbers for BP treated with DMSO for 16 h (left split) and ML7 for 4 h, followed by rescue for 12 h (right split). The dotted line represents mean. **J** Positions of HC kinocilia in polar coordinates from BP treated with DMSO (red) and ML7 (blue) for 4 h followed by rescue for 12 h. Arrows represent respective mean orientation. $N = 198/149$ (DMSO/ML7). **K** Relative fluctuations in junctional length over 400 min for HC-SC (red) and SC-SC (grey) junctions in DMSO and ML7 treated explants. $N = 474/479$ (HC-SC/SC-SC, control) and 327/472 (ML7). ns = $p > 0.05$ non-significant, $^{**}p < 0.01$, $^{****}p < 0.0001$, Unpaired Two-tailed T-test. Scale bar: 5 μm. Image orientation: D – right, S – up. For details, see methods, Supplementary Tables 4 and 8.

Since HC-SC junctions only express p-RLC, we re-assessed its localisation. We found that at E8, when HCs are apolar, p-RLC was uniformly distributed and found equally on all HC-SC junctions (Supplementary Fig. 7C). From E10, as HC polarity developed, p-RLC was enriched on HC-SC junctions away from the kinocilium (Fig. 4A, B). This asymmetry vanished by E12 (Supplementary Fig. 7D). Live imaging of E10 BP explants revealed that HC-SC junctions away from the kinocilium, which are enriched with p-RLC, showed significantly higher relative length fluctuations than those close to the kinocilium (Fig. 4C).

To confirm that LGN-Gαi is involved in p-RLC asymmetry, we cultured E10 BP explants with pertussis toxin (PTX), an inhibitor of Gαi. Similar to mouse[30,31], PTX treatment increased the c.s.d. of HC polarity in BP explants (Supplementary Fig. 7E, F; Supplementary Table 2). However, we did not observe significant changes in the HC-HC contacts, and HC hexatic order (Supplementary Fig. 7E, G, H). Importantly, PTX inhibition also resulted in the loss of asymmetric p-RLC expression on HC-SC junctions and the differences in junctional activity (Fig. 4C; Supplementary Fig. 7I, J, and Supplementary Movie 6). Together, these results show that the LGN-Gαi complex regulates asymmetries in the mechanics of HC-SC junctions, potentially coupling HC polarity to junctional mechanics.

As HC polarity is aligned to the BP tissue axis, the mechanical asymmetry of the HC, driven by p-RLC, must also be aligned. Tissue-wide alignment emerges even though HCs do not contact other HCs. Thus, their coordination could be coupled to intervening SCs, to an extrinsic tissue-wide cue or to a combination of both. Our observation that inhibition of SC-SC localised pp-RLC through ML-7 could reversibly perturb planar polarity suggested that coupling between HCs could be mediated, in part, through SCs and their junctional mechanics.

To understand if junctional mechanics may couple HC mechanical asymmetry to the tissue axis, we re-examined the localisation of pp-RLC on SC-SC junctions. At E10, SC-SC junctions aligned with the P-D axis (<30° to the P-D axis) showed significantly higher levels of pp-RLC than non-aligned (>30° to the P-D axis) SC-SC junctions (Fig. 4D, E; Supplementary Fig. 8A). We did not observe these orientational dependencies at E8 or E12 (Supplementary Fig. 8B–D). We measured the length fluctuations of the two populations in E10 live imaged BP and found that those SC-SC junctions within 30° of the P-D axis showed significantly less fluctuations than those that were greater than 30° (Fig. 4F) suggesting SC-SC junctions that are aligned to the tissue axis have a higher contractility.

https://doi.org/10.1038/s41467-025-58557-0

Following these observations, we incorporated the tuned junctional mechanics found on HC-SC and SC-SC junctions into the heterogeneous vertex-model. First, we introduced an orientation φ_α, denoting HC polarity, and considered a dependence of HC-SC junctional contractility on its orientation $\psi_{i,j}$ relative to HC polarity, where junctions far from the kinocilium are more contractile (Fig. 4G and see

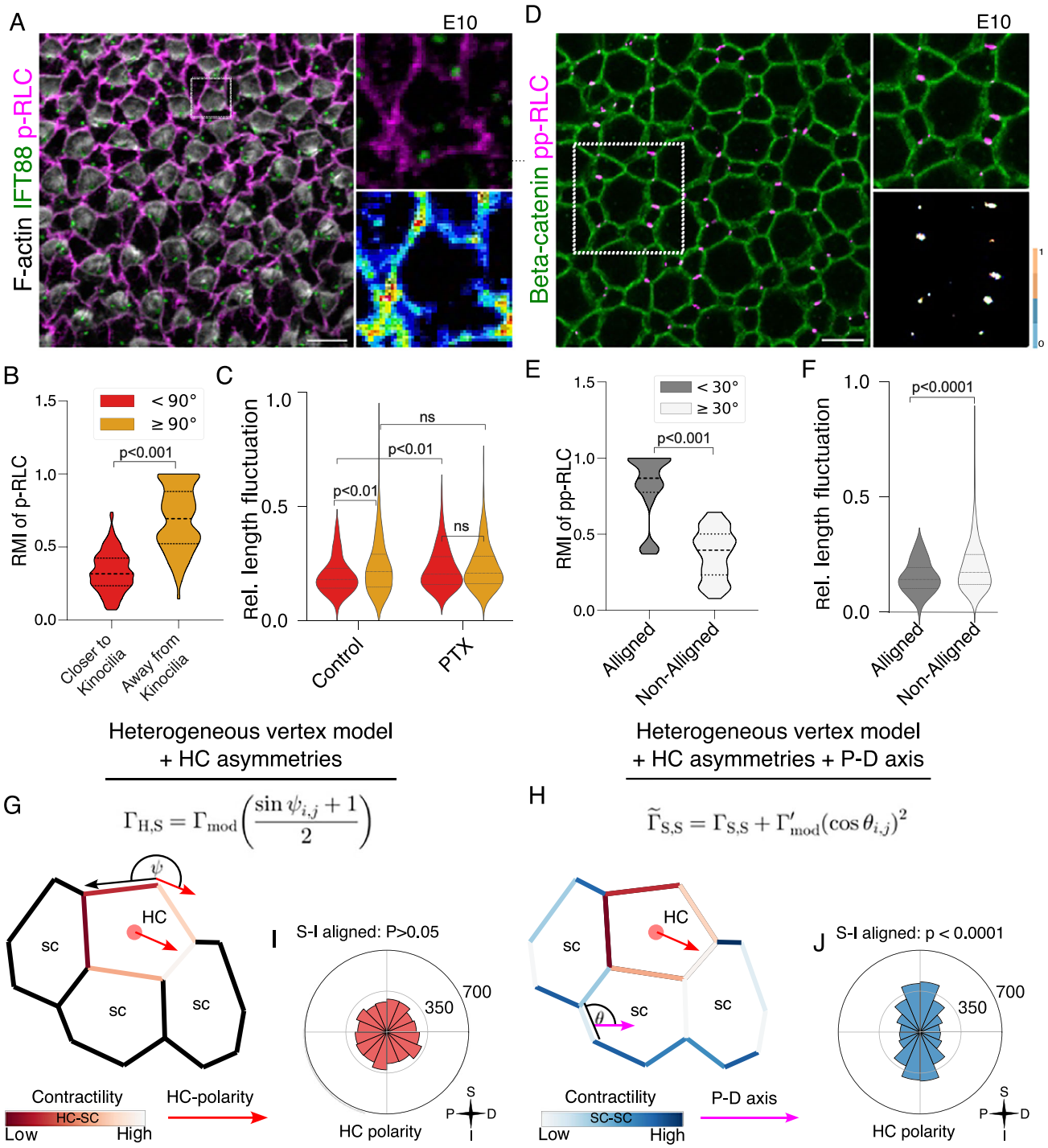

Fig. 4 | Tuning of junctional heterogeneity generates planar polarity in BP. **A** E10 BP stained with F-actin (grey), IFT88 (green) and p-RLC (magenta and 16 colours LUT). $N = 5$ embryos. **B** Relative Mean Intensity (RMI) of p-RLC on HC-SC junctions closer (angular distance <90°, in red) and away (angular distance ≥90°, in yellow) from kinocilia. $N = 203/202$ (closer/away). **C** Relative length fluctuation for HC-SC junctions closer (angular distance <90°, in red) and away (angular distance ≥90°, in yellow) from kinocilia in live imaged control and PTX treated BP. $N = 98/98$ (<90°/≥ 90°, control) and 135/131 (<90°/≥90°, PTX). **D** E10 BP stained with β-catenin (green) and pp-RLC (magenta and 16 colours LUT). $N = 6$ embryos. **E** Relative Mean Intensity (RMI) of pp-RLC on SC-SC junctions aligned (<30°) and non-aligned (≥30°) to the P-D axis. $N = 466/554$ (aligned/ non-aligned). **F** Relative length fluctuation for SC-SC junctions aligned (<30°) and non-aligned (≥30°) to the P-D axis. $N = 71/408$ (<30°/≥30°, control) and 50/441 (<30°/≥30°, PTX). **G** Schematic of the vertex model showing the asymmetries in contractility of HC-SC junctions tuned with respect to HC polarity, representing kinocilium position. **H** Schematic of the vertex model showing the asymmetries in contractility of SC-SC junctions tuned with respect to P-D axis. **I** The distribution of HC polarity considering only asymmetric contractility of HC-SC junctions. $N = 4384$. **J** The distribution of HC polarity considering both asymmetric contractility of HC-SC and SC-SC junctions. $N = 4384$. ns = $p > 0.05$ non-significant, $^{**}p < 0.01$, $^{***}p < 0.001$, $^{****}p < 0.0001$, Unpaired Two-tailed T-test. Scale bar: 5μm. Image orientation: D – right, S – up. Parameter values for (**I**–**J**) in Supplementary Table 9 (best fit).

methods for details). Second, we added a dependence of SC-SC junctional contractility on their orientation $\theta_{i,j}$ to the tissue axis, where P-D aligned junctions are more contractile (Fig. 4H). This couples the HC polarity variables to the work function of the vertex-model, reflecting LGN-Gαi signalling. Simultaneously, this coupling includes a feed-back from junctional orientation on HC orientation, which likely involves a mechanical component. The work function is then minimised with respect to the topology, vertex positions, and HC polarity. With these changes to the heterogeneous vertex-model, we observed that the individual polarities of HC were able to orient along the S-I axis, orthogonal to the tissue axis. Here, individual HCs pointed either in the superior or inferior direction with equal probability (nematic orientation) (Fig. 4I, J; Supplementary Movie 7). A closer investigation of our simulations revealed that the more contractile HC-SC junctions, farther away from the putative kinocilium position, aligned with the more contractile SC-SC junctions along the horizontal axis, together forming extended horizontal chains of higher contractility (Supplementary Fig. 8A, E). It is the emergence of these supracellular contractile junctions that leads to the alignment of HC in our simulations. The alignment of HC polarity was more pronounced with stronger SC-SC contractility along the tissue axis and did not emerge in its absence (Fig. 4I, J). Moreover, the alignment was dependent on positional order in simulations: It was dramatically reduced in those HCs that contact other HCs following perturbation of the mechanics underlying positional order (homogeneous vertex model, Supplementary Fig. 8F), in concurrence to observations from our experiments (Fig. 7H) and from data in the mouse auditory epithelium[8]. These results suggest that modulation of junctional contractility can align HC polarity across the tissue.

To understand how SC-SC junctional contractility is modulated around the P-D axis, we experimentally investigated the regulation of pp-RLC on SC-SC junctions. Many studies have implicated molecules of the planar cell polarity pathway in generating anisotropic stresses[34]. PCP proteins are indispensable for the generation of planar polarity in the mouse auditory epithelia[35–41]. In chick, Van-Gogh Like (Vangl)2 protein is enriched in the SC-SC junctions orthogonal to the HC intrinsic polarity after E12 and has been shown to regulate planar polarity of the epithelium[42]. We found that at E10, before planar polarity was established, Vangl2 already showed an enrichment at SC-SC junctions that are oriented within 30° of the P-D axis (Fig. 5A, B). Vangl2 distribution resembled that of pp-RLC (Fig. 4E), suggesting that Vangl2 is involved in pp-RLC regulation. PCP proteins have been shown to regulate actomyosin contractility[43,44]. This activation can occur through the activation of the Rho small GTPase[43,45,46], with pathways between PCP proteins and RLC activation elucidated in ommatidial rotation[43], elongation of the notochord in ascidians[47], convergence and extension during Xenopus gastrulation[48], closure of the neural tube[25], and invagination of the otic placode[49]. We found that Vangl2 colocalised with both the GTP-bound (active) form of RhoA and pp-RLC at SC-SC boundaries (Supplementary Fig. 9A–D). To test whether Vangl2 regulates pp-RLC phosphorylation on SC-SC junctions, we electroporated Vangl2-gRNA/Cas9, together with an eGFP tracer plasmid, into the otic vesicle at E3.5 to delete the Vangl2 gene and analysed the BP at E12. We observed a significant down-regulation of pp-RLC at SC-SC junctions in electroporated patches (Fig. 5C). Similar to removing pp-RLC using ML-7, Vangl2 electroporated BP showed frequent HC-HC contacts, reduced hexatic order (0.45 compared to 0.35), and higher variance in HC polarity (38° compared to 66°) (Fig. 5D–F, Supplementary Fig. 9E), suggesting a decrease in positional order and planar polarity. This is similar to observations from mouse auditory epithelia[50,51]. This indicates that Vangl2 is necessary for aligning HC planar polarity through regulating pp-RLC in SC-SC junctions.

Our experiments suggest that mechanical asymmetries can establish positional order and HC planar polarity. However, contrary to the oriented planar polarity observed experimentally, the theoretical model with tuned contractility resulted only in a nematic alignment. This suggests that while junctional asymmetries are sufficient for nematic orientation, additional cues are required for polar HC ordering.

We first investigated other mechanical asymmetries that are found in the developing BP. HC surface area and, consequently, HC neighbour numbers show a gradient from the superior to the inferior side of the BP[12,52]. However, this is only apparent after E12, after HC polarity has become aligned. Another feature of the BP is its curvature: From E8, the BP forms an arc, with the superior edge longer than the inferior (Figs. 1A, 5H). We thus simulated a curved tissue axis, where SC-SC junctional orientation is measured with respect to the curved tissue axis (see methods for details). Curvature induces differential stretching between the inferior and superior boundary. In the curved heterogeneous vertex model, the higher contractile HC-SC junctions align to the shortened inferior edge of the BP, because of the differential stretch (Fig. 5I; Supplementary Fig. 10A–E; Supplementary Movie 8). This leads to a bias of HC polarity to the inferior side with p-RLC enriched HC-SC junctions that show higher length fluctuations (and are thus less contractile) aligned to the superior edge of HC (Fig. 4C).

Our experimental and theoretical data suggest that the tuned junctional mechanics of HC-SC and SC-SC junctions can contribute to planar polarity in the BP. These junctional asymmetries are established through biochemical signals; HC intrinsic cues establish p-RLC asymmetries in HC-SC junctions, and intercellular PCP signalling via Vangl2 directs the enrichment of pp-RLC on SC-SC junctions parallel to the tissue axis. We next asked how asymmetric Vangl2 is enriched on SC-SC junctions aligned to P-D axis. Previous studies have suggested local biochemical feedback among PCP proteins, morphogen gradients as well mechanical feedback from cortical tension and the shape of cells could modulate the localisation of PCP proteins[53,54]. In BP, we asked whether local spatial order could also contribute to the asymmetric enrichment of Vangl2. To test this, we investigated our Atoh1-gRNA electroporated BPs in which spatial order is perturbed (Supplementary Fig. 3). In control-gRNA electroporated samples, we observed high Vangl2 expression on junctions parallel to the tissue axis, while non-aligned junctions showed little to no expression (Supplementary Fig. 11A, C). In Atoh-1 gRNA electroporated patches, aligned junctions showed high levels of Vangl2. However, orthogonal junctions now showed more variable levels of Vangl2 expression (Supplementary Fig. 11B, C). This suggested a role for spatial ordering in Vangl2 asymmetry. As Atoh1-gRNA have reduced HC number, we reasoned that HC themselves may exert a non-cell autonomous effect on neighbouring SC. We asked whether HC-intrinsic signalling via Gαi could contribute to the asymmetric enrichment of Vangl2 and pp-RLC on SC-SC junctions. Inhibition of Gαi, through PTX treatment, resulted in the loss of P-D bias in both pp-RLC localisation and relative junctional length fluctuations amongst SC-SC junctions (Supplementary Figs. 11D, E, 5G). Vangl2 expression shows a significant difference between parallel and orthogonal junctions, however expression levels in aligned junctions are reduced and those in non-aligned junctions increased (Supplementary Fig. 11F, G). These observations suggest that non-cell autonomous feedback involving spatial order and biochemical cues regulate the enrichment of Vangl2.

Discussion

Previous work has shown neighbour exchange driven by junctional remodelling shapes the auditory epithelia. Our work shows that these neighbour exchanges are driven by junctional heterogeneity, which also drives the positional order and planar polarity of HC in the BP. We find that positional order is dictated by differential phospho-types of RLC governing the contractile properties of HC-SC and SC-SC junctions. Our theoretical analysis implicates the higher contractility on SC-SC junctions, driven by pp-RLC activation, is sufficient for positional ordering. The SC-specific expression of myosin light chain kinase

https://doi.org/10.1038/s41467-025-58557-0

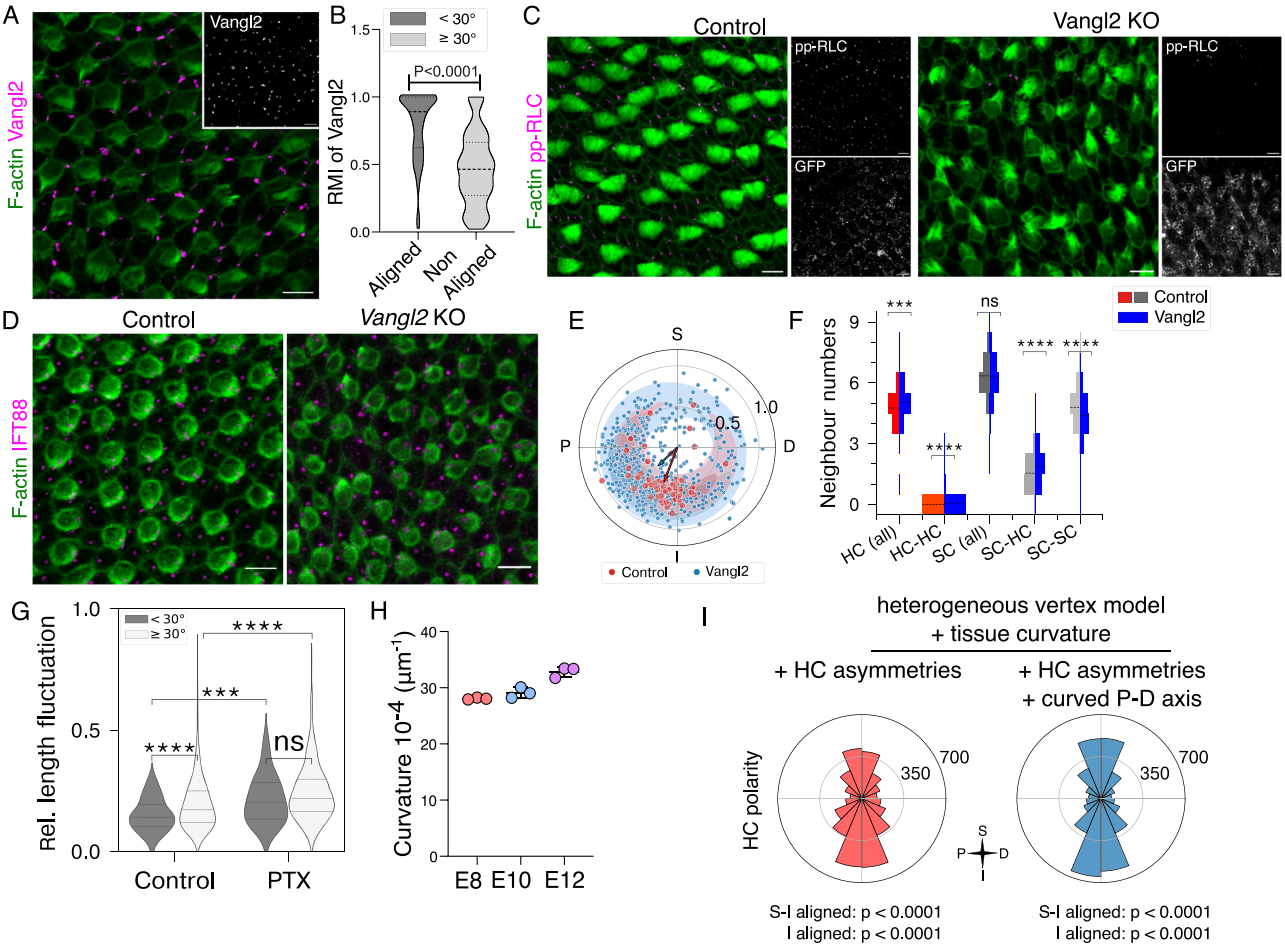

Fig. 5 | Alignment of Vangl2 driven pp-RLC to the curved P-D axis generates polarity. A E10 BP stained for F-actin (green) and Vangl2 (magenta and inset). Vangl2 is expressed on SC-SC junctions. $N = 5$ embryos. **B** Relative Mean Intensity (RMI) of Vangl2 on SC-SC junctions aligned (<30°) and non-aligned (≥30°) to the P-D axis. $N = 126/147$ (aligned/non-aligned). **C** E11 BP obtained from embryos electroporated with an empty vector (control) or an Vangl2 gRNA expressing vector, stained for GFP (green), F-actin (grey) and pp-RLC (magenta and inset). $N = 3$ embryos. **D** E12 BP obtained from embryos electroporated with an empty vector (control) or an Vangl2 gRNA expressing vector, stained for F-actin (green) and IFT88 (magenta). $N = 4$ embryos. **E** Positions of HC kinocilia in polar coordinates from control (red) and Vangl2 KO (blue) BP. $N = 63/595$ (control/Vangl2 KO). **F** Distribution of neighbour numbers for control BP (left split) and Vangl2 KO BP (right split). Here the neighbour number has been corrected for differences in HC area. See methods. 45 HC-HC contacts observed out of 751 HCs examined in Vangl2 KO compared to 0 out of 114 from in control. $N = 114/300$ (HC/SC, control) and 751/1640 (Vangl2 KO). Dotted line represents mean. **G** Relative length fluctuation for SC-SC junctions aligned (<30°) and non-aligned(≥30°) to the P-D axis in control and PTX treated explants. $N = 71/408$ (<30°/>30°, control) and 50/441 (30°/>30°, PTX). **H** Mean curvature of BP from E8 to E12. $N = 3$ embryos. Bars represent std dev. **I** The distribution of HC polarity in the asymmetric vertex model, considering a curved P-D axis with only asymmetric contractility of HC-SC junctions (red) and with both asymmetric contractility of HC-SC and SC-SC junctions (blue). Polarities are measured w.r.t. the tangent of the curved P-D axis. $N = 4384$ each. Statistics: ns = $p > 0.05$ non-significant, $^{**}p < 0.01$, $^{***}p < 0.001$, $^{****}p < 0.0001$, Unpaired Two-tailed T-test. Scale bar: 5µm. Image orientation: D – right, S – up. Experimental values in Supplementary Table 4. Parameter values for (**I**) in Supplementary Table 10 (best fit).

points to a cell-type-specific genetic programme that leads to this activation. Indeed, by merely inhibiting MLCK, SCs behave mechanically like HCs and positional order is impaired. Additional cellular properties, such as adhesion, may also contribute to positional ordering[7,9]. However, our theoretical analysis suggests that the main role of adhesion is to prevent the formation of residual HC-HC contacts and thereby refine hexatic order during cell rearrangements.

While junctional heterogeneity has been invoked as a mechanism that refines spatial patterning in the mouse organ of Corti[7], it has not been previously linked to planar polarity. During positional ordering, we find that a second layer of regulation establishes the force patterns that can order polarity across the auditory epithelium. This tunes contractility during a 2-day time window between E10 and E12, biasing pp-RLC on SC-SC junctions aligned to the P-D axis and p-RLC on HC-SC junctions furthest from the kinocilium. Vangl2, a core PCP protein, becomes enriched on P-D-oriented SC-SC junctions, and it is likely that its bias to these junctions provides the tissue reference axis to which forces are organised. What establishes this tissue reference axis? All models of planar cell polarity suggest the presence of an upstream module that orients polarity to the tissue axis[55,56]. Traction force provided by the growing tectorial membrane has been proposed to provide one such cue[4]. Two lines of evidence argue against this. The first is data from the alligator, where part of the BP is not covered by the tectorial membrane[57]. Hair cells from this region are still ordered. The second is data from mutant mice in which tectorial membrane components are perturbed[58,59]. These do not show such orientational ordering defects. The observation that the alignment of HC polarity in mouse auditory epithelia is rescued in the absence of Vangl2 suggests a possible role of biochemical gradients in organising the tissue reference axis[50]. In the inner ear, gradients across the proximal-distal axis are known, and involve BMP and retinoic acid signalling. However, perturbations of either do not affect polarity alignment[60,61]. Studies in the mouse organ of Corti and zebrafish lateral line suggest a role for Wnt signalling in defining the orthogonal, superior-inferior axis. Here,

perturbations of Wnt and its interacting proteins affect polarity alignment[62–68]. In chick, Wnt9a is expressed on the superior side of the BP in the E8 BP[69]. Thus, a prediction would be that Wnt signalling establishes the P-D bias of SC-SC junction of Vangl2 expression in chick. In mouse mutants for Wnt5a and Wnt7b, as well as where Wnt secretion is affected, some core PCP proteins fail to align to the S-I axis, although Vangl1/2 localisation is unaffected[65,66,68].

In our vertex model, the tuned heterogeneity of SC-SC junctions along the P-D axis aligns HC mechanical polarity. However, HCs in the simulated BP show an equal preference for the superior or inferior direction (Supplementary Fig. 8). By incorporating the curvature of the BP, our models can predispose HC to adopt one direction over the other. However, in our models, alignment requires sustained, tuned junctional heterogeneity. This is in contrast with our experimental observations where after E12 tuned heterogeneity is diminished. Thus, it is likely that additional biochemical cues are required to refine and stabilise HC polarity after E12. These could be the gradients that define the S-I axis or even other downstream pathways of the intercellular PCP proteins. This may also provide a mechanism for polarity in the vestibular systems. In the maculae of the inner ear, HCs are organised into two domains defined by the presence or absence of the transcription factor Emx2[70]. Here, these domains consist of HCs pointing to a line of polarity reversal and showing a mirror-image orientation. The expression of GPR156, through the regulation by Emx2, underlies the ability of HC to adopt a reversed planar polarity[71]. From our data, we hypothesise that while tuned junctional mechanics would ensure an alignment to a reference axis, Emx2 expression would reverse the response to the biochemical signal that ensures a polar and not a nematic organisation. Such mechanical models may also underlie the ability of the zebrafish lateral line to develop and regenerate with bidirectional polarity[70–72]. Thus, our tuned heterogeneous vertex model provides an essential mechanical framework for positional order and planar polarity in multi-cell type epithelia by generating force patterns across tissues.

Methods

Animals

All chick experimental protocols were approved by the NCBS Institutional Animal Ethics Committee.

Whole mount Immunostaining

Fertilised hens eggs, from Kallinga chickens, were purchased from Central Poultry Development Organisation and Training Institute (Hesaraghatta, Bangalore, India). They were incubated horizontally at 37 °C. At the desired stage, the inner ear was dissected in ice-cold PBS (without Ca^{2+} & Mg^{2+}) as previously described[73]. They were fixed in 4% PFA (dissolved in PBS) for 1–4 h at room temperature or 4 °C overnight or 2% TCA for 20 mins at 4 °C on a shaker depending on the antibody (detail for each experiment provided in Supplementary Table 3). The fixed basilar papilla was micro-dissected in PBS, permeabilised in 0.3% PBST (Tween-20) for 20 mins at RT, and blocked in blocking buffer (10% Goat serum 1% BSA in 0.3% PBST) at RT for 2 h. BP was then incubated in primary antibodies diluted in blocking solution overnight at 4 °C in a 48-well plate. For details of antibodies, please refer to Supplementary Table 3. The samples were further washed thoroughly using PBST and further incubated in secondary antibodies (1:500), Alexa-Fluor conjugated Phalloidin (1:600) diluted in PBST for 1 h at RT. After washing, samples were counter-stained for DAPI and then mounted in Fluoroshield.

For immunostaining frozen sections, inner ear from staged embryos was dissected as above. The cochlear duct was dissected and gradually equilibrated in 10%, 20%, and 30% sucrose solution (in water) and then frozen in tissue freezing medium, and sectioned at 20 μm thickness from distal to proximal side. The proximal-distal position of the section was labelled by section number and total section obtained. Sections was then dried at 37 °C for 1 h, before washing and permeabilization with PBST (0.5% Tween-20) for 10 mins, blocked in 10% goat serum, 1% BSA diluted in PBST for 2 h. Primary antibody for Myosin7A (1:200, diluted in blocking) was incubated overnight at 4 °C. sectioned were thoroughly washed with PBST, and incubated with secondary antibodies (1:1000) and Alexa-fluor conjugated Phalloidin (1:1000) diluted in PBST. Sections were then washed and counter-stained with DAPI, mounted in fluoroshield, and imaged using a confocal microscope.

Imaging

All confocal images were taken using Olympus FV 3000 inverted microscope at CIFF NCBS. Otherwise specified images were taken using 60X oil immersion objective of numerical aperture (NA) 1.42 with step size of 0.5 μm, line sequential scanning, HV values ranging between 400–500 V. Whole BP images were taken using air 10X objective of NA 0.4 with step size of 1 μm, line sequential scanning, HV values ranging between 400–500 V. It was then tiled using Fiji and Inkscape. All images are taken with 1x gain and 16bit-depth using the Olympus fluoview software. The rotation feature was used to align tissue wherever necessary, and a maximum intensity projection and merge of multiple channels was performed. For Fig. 1A, images taken at E10 and E12 are cropped and assembled using Inkscape.

CRISPR-Cas9 constructs

Atoh1 was targeted as already described[74]. For Vangl2, exon 2 and 3, common to all isoforms, were targeted. Three gRNA construct were made by cloning the following sequences into the sgRNA scaffold of pCU6.1-sgRNA vector (a gift from Tatjana Sauka-Spengler; Addgene plasmid # 92395)[75]; 1. TGGACAACGAATCGACCCGG**GGG**; 2. CGCGGAA GACGAAGACGCGT**GGG**; 3. CATGACGAACTTGTGCGACT**TGG**. PAM sequences are in bold.

In-ovo electroporation

The method is as described[73]. Briefly, eggs were incubated at 37 °C, 45% humidity for 3.5–4 Days and then windowed. Using a pair of forceps, we remove the extraembryonic membranes through the window and expose a small part of embryos around the otic vesicle. Using a glass pipette and femtojet we injected the DNA mix into the otic vesicle (for volumes of mix refer to Supplementary Table 4). We then place electrodes parallel to the dorsal-ventral axis of the spinal cord and electroporate the embryo with five pulses of 30 V and 100-ms duration each. The eggs were resealed for further incubation at 38 °C until the appropriate stage was reached.

Ex-ovo explants

Inner ears from staged embryos were dissected in filtered ice-cold PBS (without Ca^{2+} & Mg^{2+}) and cochlear duct was grown in 3D-collagen culture as previously described[73,76]. Briefly, 3 drops of collagen mix (400 μl of 3 mg/m of Rat tail collagen I, 50 μl of 10X DMEM, 30 μl of 7.5%NaHCo3 and 10 μl of HEPES) was put in each well of 4 well plate. One cochlear duct was placed in each drop and incubated for 5 min in an incubator at 37 °C. The cochlear duct was grown in DMEM supplemented with N2 and penicillin at 37 °C and 5% CO_2. Small molecular inhibitors were added in the media, ROCK inhibitor, Y-27632 (25 μM); MLCK inhibitor, ML7 (50 μM); Rho-inhibitor, CT04 (2 μg/ml); GNAi-inhibitor, PTX (250 ng/ml). After the treatment time, the samples were then washed twice with PBS and fixed using 4% paraformaldehyde for immunostaining. For wash-off and rescue experiments, the collagen culture was grown for 4 h, followed by 3 washes with HBSS, and the explant was grown further for 12-h in media without inhibitors (Supplementary Fig. 6D).

Live imaging

The cochlear duct was dissected in Ice-cold filtered PBS from staged embryos. After removing tegmentum vasculosum, the duct was put in

a collagen droplet with HC facing down, in a coverslip bottom 35 mm culture dish. Dish was kept in an incubator for 5 min and then incubated with sir-actin (50 nM) diluted in media (DMEM + N2+penicillin) for 30 mins and washed with HBSS. BP was then imaged using 60X oil immersion objective (NA 1.42) on Olympus FV3000 inverted microscope in a TYOBO incubator maintained at 5% CO_2 and 37 °C temperature. The images were acquired with a step size of 0.5 μm, with a 300 s interval with high gain voltage (550–580 V). The live imaging in the presence of inhibitors, media containing inhibitors, was added after taking 2 images of the sample.

Segmentation

For 2D morphological characterisation of the tissue we segmented the images obtained from confocal using Tissue Analyzer (TA) plugin for Fiji[77] and applied manual correction wherever necessary[78]. We then assigned cell type and cilia position based upon HCA and IFT88 staining, respectively and generated a database of cells and bonds using TA. This was further used to quantify various parameters.

For live imaging, in the absence of IFT88 staining, we inferred cilia position from the position of the fonticulus and stereocilia bundle in SiR-actin labelled HCs on HC surfaces.

Cilium quantification

In each HC, we can define a planar polarity vector from the cell's geometric centre to the position of the kinocilium's base. This vector is quantified by its length r and its angle θ to the P-D axis. The length of this vector can be normalised to the square root of the cell's area. To quantify the eccentricity of the kinocilium, we correct this vector for possible cellular elongation. The axis and magnitude of cellular elongation can be represented by a traceless symmetric tensor

$$Q = \begin{pmatrix} q_1 & q_2 \\ q_2 & -q_1 \end{pmatrix} = |q| \begin{pmatrix} \cos 2\theta & \sin 2\theta \\ \sin 2\theta & -\cos 2\theta \end{pmatrix}. \quad (2)$$

Cellular elongation was calculated from a triangulation of the cell's vertices[79]. The ratio of the long over the short axis of the such defined ellipse is given as

$$R = exp(|q|/2) \quad (3)$$

and was used to normalise the vector to the cilium. Thereby, a vector of length 1 indicates a position on the cell boundary.

Statistics of cellular polarity are given by the population resultant vector of the polarities with angles weighted by their amplitudes r_n

$$z = \sum_{n=1}^{N} r_n e^{i\theta_n} \Big/ \sum_{n=1}^{N} r_n, \quad (4)$$

which can be expressed as

$$z = \bar{r} e^{i\bar{\theta}} \quad (5)$$

with a circular variance

$$Var(z) = 1 - \bar{r} \quad (6)$$

and a circular mean $\bar{\theta}$. The circular standard deviation (CSD) is given as

$$S(z) = \sqrt{-2ln(\bar{r})} \quad (7)$$

We use the circular standard deviation to characterise the distribution of polarity orientation, prior to calculating CSD we align the axes of all images by their circular mean polarity.

Hexatic order parameter

The hexatic order parameter quantifies the angular order of proximate HCs. For every HC it can be defined as

$$\psi_6 = 1/N \sum_{n=1}^{N} e^{i6\phi_n} \quad (8)$$

where ϕ_n is the angle of the vector from the HC's centre to the centre of a next-neighbour HC to the P-D tissue axis. We correct the positions of proximate HCs to the cellular elongation of the considered HC. A hexatic arrangement of HCs that was elongated by any single axis has hexatic order $\psi_6 = 1$. We define $\psi_6 = 0$ for $N < 3$.

Neighbour number analysis

Using the database generated from TA, we quantified the number of neighbours for each cell and the identity of those neighbours using a python script.

Surface area

From the database generated from TA, we quantified the apical surface area of cells for each cell and then segregated them as HC or SC based upon HCA staining identity. We next normalized the cell area for each cell to the average cell area of the tissue.

Volume

Cryosectioned BP is stained for HC cytoplasmic marker Myosin7a. Using the cells function in Imaris we segmented the entire HCs and selected only those cells which were complete. We then quantified the volume of those HCs.

Co-localization

Using Fiji, confocal images were changed to 8-bit format. The image was then thresholded and analysed for image wide co-localization using the JaCoP plugin[80]. A separate ROI based analysis was performed on SC-SC junction. For this a ROI going through the SC-SC junction was drawn and the grey values for each channel on that line was imported to MS excel. These values were then normalized to the respective maximum intensity and that value was then used to calculate Co-localization.

Lewis' law

The Lewis' law[15] expresses a phenomenological linear relation between the average cell area and the neighbour number

$$\frac{A_n}{A} = \frac{n-2}{4}. \quad (9)$$

In segmentation of BP, we find that the SCs, but not the HCs, display this relation (Fig. S4B). Here, normalisation A was performed for individual images and cell-types, thus removing differences in cell area (e.g. increase of HC area, Supplementary Fig. 4A): at a given position and stage, HC area does not depend on polygon type, as opposed to Lewis' law, even though HC neighbour number depends on HC area across stages and positions (Fig. 1D; Supplementary Fig. 4A).

Relative intensity of RLC phosphorylation

For pp-RLC, images were taken as superior up and proximal left. A HC along with neighbouring cells, was duplicated, and we calculated angles for each SC-SC β-catenin staining and the mean intensity of pp-RLC for these junctions. We normalised the intensity values to the maximum intensity and binned the junctions with orientation to the P-D of less than 30° as "aligned" and otherwise as "not-aligned". For p-RLC, the intensity at HC-SC junctions and the angle between the kinocilium vector and the vector from the cell centre to the centre of a junction was obtained using Fiji, we then binned junctions with angle

less than 90° as closer to cilia and one with higher than 90° as away from kinocilium.

Relative bond fluctuations

We segmented cell boundaries for each time frame using TA and tracked each junction across time frames. For each junction, we quantified the mean junctional length $L_{i,j}$ and the standard deviation of junctional length $\sigma_{i,j}$ for each trajectory. We normalised the deviation to the mean junctional length and refer to this quantity as relative length fluctuations:

$$\Delta L_{i,j} = \sigma / L_{i,j}. \tag{10}$$

Junctions which are apparent in less than 5 images (25 min) were discarded.

What do length fluctuations tell us about the mechanical properties of the junction? On timescales of several hours, junctions can be considered rigid. Therefore, in a 1D approximation, we considered a single junction as an elastic spring. Due to the activity of the actomyosin complex forces act on this spring, which we denote f_p and f_{pp} for p- and pp-RLC, respectively. In an overdamped environment, changes in the length of this spring can be expressed as

$$\gamma \dot{l} = -k(l - l_0) - f_{pp} - f_p + \eta \tag{11}$$

with a damping factor γ. The first term of the right-hand side describes a linear spring with rest length l_0 and elastic modulus k. We consider fluctuations to be Gaussian white noise η with zero mean, $\langle \eta \rangle = 0$, and correlations

$$\langle \eta(t)\eta(t') \rangle = 2\Delta\delta(t - t'). \tag{12}$$

These fluctuations could be due to molecular noises in the cytoskeleton in adjacent junctions.

We assume the active forces f_p and f_{pp} to be proportional to the number of bound p-RLC and pp-RLC, N_p and N_{pp}, respectively

$$f_p = f_p^0 N_p \text{ and } f_{pp} = f_{pp}^0 N_{pp} \tag{13}$$

How the number of bound p- and pp-RLC evolves through successive phosphorylation in a bath of non-phosphorylated RLC can be described by the following equations

$$\dot{N_p} = k_p l - k_d N_p - k_{pp} N_p + k_{dp} N_{pp} \tag{14}$$

$$\dot{N_{pp}} = +k_{pp} N_p - k_{dp} N_{pp} \tag{15}$$

with the phosphorylation rates k_p and k_{pp}, and dephosphorylation rates k_d and k_{dp}, respectively.

The equilibrium-state values are

$$N_p^0 = \frac{k_p}{k_d} \cdot l \tag{16}$$

$$N_{pp}^0 = \frac{k_{pp}}{k_{kp}} N_p^0 \tag{17}$$

$$l = l_0 \left(1 + \frac{k_p}{k \cdot k_d} \left(f_p^0 + f_{pp}^0 \frac{k_{pp}}{k_{dp}}\right)\right)^{-1} \equiv L_0. \tag{18}$$

How this equilibrium state responds to small perturbations $l = L_0 + \delta l$, $N_p = N_p^0 + \delta N_p$, and $N_{pp} = N_{pp}^0 + \delta N_{pp}$ is given by the following equations

$$\delta \dot{N}_{pp} = +k_{pp}\delta N_p - k_{dp}\delta N_{pp} \tag{19}$$

$$\delta \dot{N}_p = k_p \delta l - k_d \delta N_p - k_{pp}\delta N_p + k_{dp}\delta N_{pp} \tag{20}$$

$$\gamma \dot{l} = -k\delta l - f_{pp}^0 \delta N_{pp} - f_p^0 \delta N_p + \eta. \tag{21}$$

In Fourier-space this gives

$$\delta N_{pp} = \frac{k_{pp}}{i\omega + k_{dp}} \delta N_p \tag{22}$$

$$\delta N_p = \frac{k_d}{i\omega + k_d + k_{pp} - k_{dp}\frac{k_{pp}}{i\omega + k_{dp}}} \delta l \tag{23}$$

$$\delta l = \frac{\eta}{i\omega\gamma + A_\omega} \tag{24}$$

where

$$A_\omega \equiv k + \left(f_p^0 + f_{pp}^0 \frac{k_{pp}}{(i\omega + k_{dp})} \frac{k_p (i\omega + k_{dp})}{(i\omega + k_d + k_{pp})(i\omega + k_{dp}) - k_{dp}k_{pp}} \right). \tag{25}$$

Eventually, in real space, fluctuations in spring length are given as

$$\langle \delta l(t)\delta l(t') \rangle = \frac{1}{2\pi} \int d\omega d\omega' \exp(-i(\omega t + \omega' t')) \frac{1}{i\omega\gamma + A_\omega} \frac{1}{i\omega'\gamma + A'_\omega}. \tag{26}$$

Exploiting the properties of Gaussian white noise $\langle \eta(\omega)\eta(\omega') \rangle = 2\Delta\delta(\omega + \omega')$, we obtain

$$\langle \delta l(t)\delta l(t') \rangle = \frac{1}{\pi} \int d\omega \exp(-i(\omega(t - t')) \frac{1}{i\omega\gamma + A_\omega} \frac{1}{-i\omega\gamma + A_{-\omega}}. \tag{27}$$

Numerical evaluation of this integral shows that length fluctuations decrease with an increase in the phosphorylation rate of pp-RLC, k_{pp} (Fig. S4F). Here, the number of pp-RLC is directly proportional to k_{pp}.

In other words, in this model, an enrichment of pp-RLC on SC-SC junctions results in a reduction in their length fluctuations through the increase of junctional contractility compared to HC-SC junctions.

Statistics and reproducibility

We performed two tail unpaired T-test without assuming Gaussian distribution as Mann-Whitney T-test to calculate the significance level.

The experiment presented in Fig. 1a is performed three independent times. Data associated with experiments shown in Figs. 1b, 2c, d are presented in Supplementary Table 1.

Vertex model simulations

We describe the apical surface of a monolayer of epithelial cells using the framework of the 2d vertex model[24,81]. In the vertex model each cell is described by a polygon where the edges represent cell-cell contact lines, which we call junctions in the following. The junctions end in vertices, in which three junctions intersect. We consider the

configuration of the tissue where the total force on each vertex

$$\mathbf{F}_i = -\frac{\partial W}{\partial \mathbf{R}_i} \tag{28}$$

vanishes at mechanical equilibrium. Here, $\mathbf{R}_i$ is the 2 d position of the vertex and W the work function that characterises each configuration of the tissue. The work function penalises deviations from a target apical cell surface area $A_\alpha^{(0)}$ and cell shape index $p_\alpha^{(0)}$. Here, the index α refers to a specific cell and the shape index is the ratio of the cell's perimeter P_α to the square root of the target area, $p_\alpha = \frac{P_\alpha}{\sqrt{A_\alpha^{(0)}}}$. Explicitly we write for the work function[81]

$$W = \sum_\alpha \frac{K_A}{2}\left(\frac{A_\alpha}{A_\alpha^{(0)}} - 1\right)^2 + \sum_\alpha \frac{K_S}{2}\left(p_\alpha - p_\alpha^{(0)}\right)^2. \tag{29}$$

Here, the parameters K_A and K_S are elastic constants. Typical values for all parameters are displayed in Table S5.

To account for the presence of two different cell-types, hair (H) and supporting (S) cells, we explicitly allow the parameter values $A_\alpha^{(0)}$ and $p_\alpha^{(0)}$ to depend on cell types: $A_\alpha^{(0)} = A_H^{(0)}$ for HCs and $A_\alpha^{(0)} = A_S^{(0)}$ for SCs. Furthermore, we extend this homogeneous work function to include heterotypic cell-cell surface interactions and junctional contractility,

$$W^{het} = W^{hom} + \sum_{\langle i,j\rangle} \Lambda_{i,j} l_{ij} + \sum_{\langle i,j\rangle} \Gamma_{i,j} l_{ij}^2, \tag{30}$$

where l_{ij} is the length of the junction $\langle i,j\rangle$ connecting the vertices i and j. These terms permit to consider differences in tension $\Lambda_{i,j}$ and contractility $\Gamma_{i,j}$ between the different junctions. Here, we consider all junctions of the same type to have identical values, explicitly $\Lambda_{i,j} = \Lambda_{H,H}$ for junctions connecting two HCs, $\Lambda_{i,j} = \Lambda_{H,S} = \Lambda_{S,H}$ for HC-SC junctions, and $\Lambda_{i,j} = \Lambda_{S,S}$ for SC-SC junctions, and similarly for $\Gamma_{i,j}$.

Mechanical equilibrium is determined using a steepest-descent algorithm. In each step, we allow for changes in the work function caused by remodelling of the cellular structure defined by the junctions. Explicitly, whenever the length of a cell-cell junction is shorter than a threshold length $l_{\min}$, a so called T1 transition occurs. In this transition, the junction is removed and a new junction of length $l = d\, l_{\min}$ is created in orthogonal orientation[82]. We discard transitions that increase the work function. Likewise, if a cell's surface area shrinks below a threshold value $A_{\min}$ and the cell is composed of 3 vertices, then it is removed and replaced by a single vertex, which is often referred to as a T2 transition. Note that in our simulations no T2 transitions occur.

Remodelling of the cellular structure permits a viscous relaxation of the tissue after persistent deformation and occurs on a long timescale. Fast deformations typically result in an elastic response without remodelling of the cellular structure[81,83]. To obtain smooth stress-strain curves, we relax the accumulated strain by introducing fluctuations in the system. We follow Duclut et al.[83] and adopt fluctuations in the bond tension parameter, where the dynamics of individual bonds are described by an Ornstein-Uhlenbeck process,

$$\frac{\mathrm{d}\Lambda_{\mathrm{i,j}}}{\mathrm{dt}} = -\frac{1}{\tau_\Lambda}\left(\Lambda_{\mathrm{i,j}}(\mathrm{t}) - \Lambda_{\mathrm{i,j}}^{(0)}\right) + \Delta\Lambda\sqrt{2/\tau_\Lambda}\,\Xi_{\mathrm{i,j}}(\mathrm{t}). \tag{31}$$

Here the first term on the right-hand side describes a relaxation of the parameter to a mean value $\Lambda_{i,j}$ over a timescale given by the characteristic time τ_Λ. The second term comprises the Gaussian white noise $\Xi_{i,j}(t)$ with zero mean $\langle \Xi_{i,j}(t)\rangle = 0$ and correlations $\langle \Xi_{i,j}(t)\Xi_{k,l}(t')\rangle = \delta\langle i,j\rangle,\langle k,l\rangle\delta(t-t')$, with $\delta\langle i,j\rangle,\langle k,l\rangle = 1$ when $\langle i,j\rangle$ and $\langle k,l\rangle$ describe the same junction and 0 otherwise. The magnitude of the fluctuations is captured by the parameter $\Delta\Lambda$. We have chosen the characteristic time scale of the fluctuations τ_Λ to be much larger than the elastic relaxation time of the work function.

The initial state of our model is generated from an arrangement of 4×4 hexagonal cells in a periodic domain with area $A_{\mathrm{domain}} = N_0 A_\alpha$ such that the cells fit together with no area constraint. Initially, no heterogeneities are considered. The cells undergo cyclic cell division until the system is composed of N cells. In a cycle, every cell is divided along a randomly oriented axis through the cell's centre, giving rise to two daughter cells that inherit the parameters of the mother cell. The size of the periodic domain is adjusted to accommodate the newly created cells while maintaining its aspect ratio. Prior to the next cycle, the work function is equilibrated. Once the targeted number of cells is attained, we label N_{H} random cells as HC and the remaining cells as SC.

Studying the effect of junctional heterogeneities

Experimentally, we observed increased contractility in SC-SC junctions compared to SC-HC junctions. We, therefore explore the effect of the junctional contractility on the arrangement of cells. Our experimental data suggests an increased junctional contractility, which is traditionally represented by the term $\sum_{<i,j>}\Gamma_{\{i,j\}} l_{i,j}^2$ in the vertex-model description and hence the parameter $\Gamma_{\{i,j\}}$.

In our random arrangement of HCs and SCs, we explore the effect of SC-SC junctional contractility $\Gamma_{S,S} \geq 0 = \Gamma_{S,H}$ on the arrangement of cells. For increasing SC-SC contractility, we observed a reduction of the HC-neighbour number (Supplementary Fig. 4H). For $\Gamma_{S,S} = 0.03$, we find a best fit with HC-neighbour numbers in E10 BP (Supplementary Fig. 4I). In agreement with Euler's formula for planar graphs, the global average of cell-neighbour numbers remains 6 and hence we observe an increase in SC-neighbour number.

To confirm that pp-RLC alters the contractility of SC-SC junctions, we repeated the simulations with increased values of the junctional tension $\Lambda_{S,S}$. We find that junctional tension $\Lambda_{S,S}$ only has weak influence on the HC-neighbour number (Supplementary Fig. 4H–I). Indeed, in the absence of heterogeneous junctional tension $\Gamma_{S,S} = 0$, the HCs are indistinguishable from SCs by their neighbour number. However, at larger $\Gamma_{S,S}$, junctional tension opposes the reduction of HC-neighbour number, possibly through changing the rheology of the tissue[24,83].

It is known that differential interfacial tension ($\lambda_{A,A} \approx \lambda_{A,B} > \lambda_{B,B}$) and high interfacial tension ($\lambda_{A,B} > \lambda_{A,A}$ and $\lambda_{A,B} > \lambda_{B,B}$) between two types of cells A and B lead to the sorting of the two cell types into two separate aggregates, through minimisation of the interface length of aggregates A and B[84]. In the simulated case $\lambda_{S,S} > \lambda_{H,S} = \lambda_{H,H}$, we observe a decrease in SC-HC interface length in agreement with the results from sorting at ectoderm-mesoderm boundaries in *Xenopus*[85]. Similarly, we found a decrease of SC-HC interface length for an increase of SC-SC contractility. Interestingly, due to the low number of HCs (20–30% vs 50% in Canty et al.[85]) we observed that the number of HCs neighbouring other HCs reduced drastically for more contractile or more tensile SC-SC junctions. This reduction in HC-HC contacts can be likewise observed for increased HC-HC tension $\lambda_{H,H} > \lambda_{H,S} = \lambda_{S,S}$.

Due to the additional effect of SC-SC junctional contractility on the HC-neighbour number that cannot be described by heterogeneous junctional tension, we concluded that pp-RLC is primarily altering junctional contractility. However, unlike in BP, in simulations with only SC-SC junctional contractility about 5% of HCs retain a HC neighbour. We chose to consider additional SC-SC tension and call this model heterogeneous vertex-model, where parameters have been fitted to best describe BP (see Supplementary Tables 5 and 6 for parameter values). The following results are comparable for a study with the contractile SC-SC junctions and tensile HC-HC junctions.

Incorporating HC area increase

To incorporate differential changes in cell area, we perform the following protocol. First, we initialise N cells in a random tissue and assign randomly $N_H = \rho_H N$ hair cells. According to the junctional types, we assign heterogeneities on the bond tension $\Lambda_{i,j}$ and contractility $\Gamma_{i,j}$ parameters and relax the system over timescales longer than the viscous relaxation time. We compensate the additional stiffness of the junctions due to these parameters by an increase in the bond tension fluctuation amplitude $\Delta\Lambda$ so that all simulations show similar levels of bond remodelling induced by fluctuations. This is the $t = 0$ initial configuration. In this configuration, HCs and SCs have equal target area $A_H^{(0)} = A_S^{(0)} = 1$. We then increment the target area of hair cells by ΔA_H every 20 steps, while minimising the work function. At all times, the target area of SC is calculated from the conservation of the total domain size,

$$\sum_\alpha A_\alpha^{(0)}(t) = N_H A_H^{(0)}(t) + N_S A_S^{(0)}(t) = N = \text{const.} \tag{32}$$

We consider a maximum simulation period of 60 000 τ_Λ (15 000 τ_Λ) over which HC area increases to 4 times (decreases to 1/4) its original value (Supplementary Fig. 5D). We abort those simulations where the T2 transition criterion of cell extrusion is met in individual cells. Typical values for specific parameters are displayed in Supplementary Table 7. We compare vertex model configurations to images from the BP where the normalised HC area is the most similar (Supplementary Figs. 4A, 5D).

Studying the effects of inhibition of heterogeneities

To mimic the experiments on inhibition of junctional heterogeneities, we again initialise N cells in a random tissue with a minimal number of HC-HC contacts. We consider two sets of simulations, a homogeneous and a heterogeneous arrangement of junction parameters. The heterogeneity now is only due to differences in junctional contractility $\Gamma_{i,j}$. We minimise the work function in the presence of bond tension fluctuations over a period of 5000 τ_Λ, then remove heterogeneous junctional contractility from all junctions and continue minimisation for an additional 5000 τ_Λ, and eventually, we reintroduce junctional heterogeneity with the original values and continue. Typical values for specific parameters are displayed in Supplementary Table 8.

Incorporating asymmetric junction mechanics

We introduce a systematic angular modulation of the junctional contractility parameters to consider junctional asymmetries in the vertex model. For convenience, we add different aspects of the junctional mechanics step by step. First, we prepared a simulated tissue of HCs and SCs using our heterogeneous vertex-model. To include HC polarity, we assigned every HC a random orientation ϕ_α. We measure the angle $\psi_{i,i+1} \in [0, 2\pi)$ between HC orientation and an HC junction $\langle i, i+1\rangle$, where we have labelled the HC vertices in anti-clockwise order with i and $i+1$ being two consecutive vertices. We consider the additional contractility on HC-SC junctions as

$$W_{H,S}^{\text{mod}} = \sum_{\langle i,j\rangle \in \{H-S\}} \Gamma_{\text{mod}} \left(\frac{\sin \psi_{i,j} + 1}{2}\right) l_{i,j}^2 \tag{33}$$

In this formulation, the HC orientations ϕ_α enter the work function. We minimise the work function with respect to topology (T1 and T2 transitions), positions of vertices $\mathbf{R}_i$, and HC orientations ϕ_α in the absence of line-tension fluctuations.

Next, we include the asymmetries in SC-SC junctional contractility. To do so, we measured the angle $\theta_{i,j}$ of the junction to the tissue axis and assign the additional contractility

$$W_{S,S}^{\text{mod}} = \sum_{\langle i,j\rangle \in \{S-S\}} \Gamma'_{S,S} \cos^2\left(\theta_{i,j}\right) l_{i,j}^2. \tag{34}$$

Again, we minimise the vertex model with respect to topology (T1 and T2 transitions), positions of vertices $\mathbf{R}_i$, and HC orientations ϕ_α in the absence of line-tension fluctuations. The parameter values we used are displayed in Supplementary Table 9.

Studying the influence of a curved P-D axis

To consider the influence of the curvature of the P-D axis in the previous simulation, we use non-periodic fixed boundary conditions. Precisely, we consider an initial rectangular arrangement of 48 by 22 hexagonal cells and map every vertex to a position within an arc segment. We measure the curvature at the midpoint of the segment of arc length $48\sqrt{A_0}$ and width 22 $\sqrt{A_0}$ in radial direction. In this arrangement, we allow all vertices on the boundary to move only in tangential direction along the boundary in a direction norm and perform the same steps as in the previous simulation. Note that during the first relaxation, T1 transitions are frequent. We measure the HC orientations ϕ_α with respect to the local tangent of the arc and exclude the boundary layer of cells from our analysis quantifying overall polarity.

We quantify the nematic alignment of HC orientation using a fraction of S-I orientated HCs

$$f_{nematic} = \frac{N_I + N_S}{N_{HC}}, \tag{35}$$

with the numbers N_I and N_S of inferior and superior oriented HCs, respectively, and N_{HC} the total number of HCs (Fig. S10A-B). A high fraction $f_{\text{nematic}} > 0.5$ indicates that S and I orientations are more frequent than P and D orientations. We calculate the probability that S and I versus P and D orientations are randomly drawn from a binomial distribution. Similarly, we quantify the polar alignment of HC orientation using the fraction of I oriented HCs (Supplementary Fig. 10C-D)

$$f_{polar} = \frac{N_I}{N_S}. \tag{36}$$

In Figure S10A–D we systematically study the effect of asymmetric contractility of HC-SC junctions (parameter $\Gamma_{H,S}$), axial SC-SC contractility (parameter $\Gamma'_{S,S}$), and tissue curvature κ. We find that in the presence of axial SC-SC contractility, HC orientation is biased for a nematic S-I orientation (Fig. 4I, J; Supplementary Figs. S8E, S10A). The bias increases with the amplitude of axial SC-SC contractility modulation $\Gamma'_{S,S}$ (Supplementary Fig. 10B). This preferential nematic orientation is, in the presence of tissue curvature, biased to a S or I orientation, dependent on the sign of asymmetric HC-SC junctional contractility (Fig. 5I; Supplementary Fig. S10C–E).

The parameter values we used are displayed in Supplementary Table 10.

Simulation and evaluation framework

The above-described vertex model is implemented within the *Utopia* modelling framework for complex and adaptive systems[86]. Data handling and evaluation are performed using *dantro*[87]. See also www.utopia-project.org.

Euler's polyhedron formula

Euler, 1758[88] establishes a relationship between the number of vertices V, faces F, and edges E, $V + F - E = 0$. Constraining to topology to allow only 3-fold vertices results in a relationship between V and E, $E = 3/2V$. Hence, considering a tissue of N cells:

$$2/3E + N - E = 0 \iff E = 3N \Rightarrow 2\frac{E}{N} = 6. \tag{37}$$

Reporting summary
Further information on research design is available in the Nature Portfolio Reporting Summary linked to this article.

Data availability
Segmented data is available on Zenodo: https://doi.org/10.5281/zenodo.14917594.

Code availability
Codes used to analyse data and perform simulations are available on Zenodo: https://doi.org/10.5281/zenodo.14917594.

References

1. Deans, M. R. Conserved and divergent principles of planar polarity revealed by hair cell development and function. *Front. Neurosci.* **15**, 742391 (2021).
2. Yamamoto, N., Okano, T., Ma, X., Adelstein, R. S. & Kelley, M. W. Myosin II regulates extension, growth and patterning in the mammalian cochlear duct. *Development* **136**, 1977–1986 (2009).
3. Driver, E. C., Northrop, A. & Kelley, M. W. Cell migration, intercalation and growth regulate mammalian cochlear extension. *Development* **144**, 3766–3776 (2017).
4. Cotanche, D. A. & Corwin, J. T. Stereociliary bundles reorient during hair cell development and regeneration in the chick cochlea. *Hear Res.* **52**, 379–402 (1991).
5. Aigouy, B. et al. Cell flow reorients the axis of planar polarity in the wing epithelium of Drosophila. *Cell* **142**, 773–786 (2010).
6. Etournay, R. et al. Interplay of cell dynamics and epithelial tension during morphogenesis of the Drosophila pupal wing. *eLife* **4**, e07090 (2015).
7. Cohen, R. et al. Mechanical forces drive ordered patterning of hair cells in the mammalian inner ear. *Nat. Commun.* **11**, 5137 (2020).
8. Fukuda, T. et al. Aberrant cochlear hair cell attachments caused by Nectin-3 deficiency result in hair bundle abnormalities. *Development* **141**, 399–409 (2014).
9. Togashi, H. et al. Nectins establish a checkerboard-like cellular pattern in the auditory epithelium. *Science* **333**, 1144–1147 (2011).
10. Goodyear, R., Holley, M. & Richardson, G. Hair and supporting-cell differentiation during the development of the avian inner ear. *J. Comp. Neurol.* **351**, 81–93 (1995).
11. Jones, C. et al. Ciliary proteins link basal body polarization to planar cell polarity regulation. *Nat. Genet* **40**, 69–77 (2008).
12. Goodyear, R. & Richardson, G. Pattern formation in the basilar papilla: evidence for cell rearrangement. *J. Neurosci.* **17**, 6289–6301 (1997).
13. Bermingham, N. A. et al. Math1: an essential gene for the generation of inner ear hair cells. *Science* **284**, 1837–1841 (1999).
14. Mulvaney, J. F., Amemiya, Y., Freeman, S. D., Ladher, R. K. & Dabdoub, A. Molecular cloning and functional characterisation of chicken Atonal homologue 1: a comparison with human Atoh1. *Biol. Cell* **107**, 41–60 (2015).
15. Lewis, F. T. The effect of cell division on the shape and size of hexagonal cells. *Anat. Rec.* **33**, 331–355 (1926).
16. Katayama, A. & Corwin, J. T. Cell production in the chicken cochlea. *J. Comp. Neurol.* **281**, 129–135 (1989).
17. Vicente-Manzanares, M., Ma, X., Adelstein, R. S. & Horwitz, A. R. Non-muscle myosin II takes centre stage in cell adhesion and migration. *Nat. Rev. Mol. Cell Biol.* **10**, 778–790 (2009).
18. Vicente-Manzanares, M. & Horwitz, A. R. Myosin light chain mono- and di-phosphorylation differentially regulate adhesion and polarity in migrating cells. *Biochem Biophys. Res Commun.* **402**, 537–542 (2010).
19. Ikebe, M. & Hartshorne, D. J. Phosphorylation of smooth muscle myosin at two distinct sites by myosin light chain kinase. *J. Biol. Chem.* **260**, 10027–10031 (1985).
20. Ikebe, M., Koretz, J. & Hartshorne, D. J. Effects of phosphorylation of light chain residues threonine 18 and serine 19 on the properties and conformation of smooth muscle myosin. *J. Biol. Chem.* **263**, 6432–6437 (1988).
21. Mizutani, T., Haga, H., Koyama, Y., Takahashi, M. & Kawabata, K. Diphosphorylation of the myosin regulatory light chain enhances the tension acting on stress fibers in fibroblasts. *J. Cell Physiol.* **209**, 726–731 (2006).
22. Juanes-García A., Llorente-González C., Vicente-Manzanares M. Nonmuscle Myosin II. In: *Encyclopedia of Signaling Molecules* (ed Choi S.). Springer International Publishing (2018).
23. Spudich, J. A. The myosin swinging cross-bridge model. *Nat. Rev. Mol. Cell Biol.* **2**, 387–392 (2001).
24. Farhadifar, R., Roper, J. C., Aigouy, B., Eaton, S. & Julicher, F. The influence of cell mechanics, cell-cell interactions, and proliferation on epithelial packing. *Curr. Biol.* **17**, 2095–2104 (2007).
25. Nishimura, T., Honda, H. & Takeichi, M. Planar cell polarity links axes of spatial dynamics in neural-tube closure. *Cell* **149**, 1084–1097 (2012).
26. Nagai, T. & Honda, H. Computer simulation of wound closure in epithelial tissues: cell-basal-lamina adhesion. *Phys. Rev. E Stat. Nonlin Soft Matter Phys.* **80**, 061903 (2009).
27. Salbreux, G., Barthel, L. K., Raymond, P. A. & Lubensky, D. K. Coupling mechanical deformations and planar cell polarity to create regular patterns in the zebrafish retina. *PLoS Comput Biol.* **8**, e1002618 (2012).
28. Uehata, M. et al. Calcium sensitization of smooth muscle mediated by a Rho-associated protein kinase in hypertension. *Nature* **389**, 990–994 (1997).
29. Saitoh, M., Ishikawa, T., Matsushima, S., Naka, M. & Hidaka, H. Selective inhibition of catalytic activity of smooth muscle myosin light chain kinase. *J. Biol. Chem.* **262**, 7796–7801 (1987).
30. Ezan, J. et al. Primary cilium migration depends on G-protein signalling control of subapical cytoskeleton. *Nat. Cell Biol.* **15**, 1107–1115 (2013).
31. Tarchini, B., Jolicoeur, C. & Cayouette, M. A molecular blueprint at the apical surface establishes planar asymmetry in cochlear hair cells. *Dev. Cell* **27**, 88–102 (2013).
32. Bhonker, Y. et al. The GPSM2/LGN GoLoco motifs are essential for hearing. *Mamm. Genome.: Off. J. Int. Mamm. Genome. Soc.* **27**, 29–46 (2016).
33. Sugioka, K. & Bowerman, B. Combinatorial contact cues specify cell division orientation by directing cortical myosin flows. *Dev. Cell* **46**, 257–270 e255 (2018).
34. Pare, A. C. & Zallen, J. A. Cellular, molecular, and biophysical control of epithelial cell intercalation. *Curr. Top. Dev. Biol.* **136**, 167–193 (2020).
35. Montcouquiol, M. et al. Identification of Vangl2 and Scrb1 as planar polarity genes in mammals. *Nature* **423**, 173–177 (2003).
36. Curtin, J. A. et al. Mutation of Celsr1 disrupts planar polarity of inner ear hair cells and causes severe neural tube defects in the mouse. *Curr. Biol.* **13**, 1129–1133 (2003).
37. Yin, H., Copley, C. O., Goodrich, L. V. & Deans, M. R. Comparison of phenotypes between different vangl2 mutants demonstrates dominant effects of the Looptail mutation during hair cell development. *PLoS One* **7**, e31988 (2012).
38. Etheridge, S. L. et al. Murine dishevelled 3 functions in redundant pathways with dishevelled 1 and 2 in normal cardiac outflow tract, cochlea, and neural tube development. *PLoS Genet.* **4**, e1000259 (2008).

39. Wang, J. et al. Regulation of polarized extension and planar cell polarity in the cochlea by the vertebrate PCP pathway. *Nat. Genet.* **37**, 980–985 (2005).
40. Wang, Y., Guo, N. & Nathans, J. The role of Frizzled3 and Frizzled6 in neural tube closure and in the planar polarity of inner-ear sensory hair cells. *J. Neurosci.* **26**, 2147–2156 (2006).
41. Stoller, M. L., Roman, O. Jr. & Deans, M. R. Domineering non-autonomy in Vangl1;Vangl2 double mutants demonstrates intercellular PCP signaling in the vertebrate inner ear. *Dev. Biol.* **437**, 17–26 (2018).
42. Sienknecht, U. J., Anderson, B. K., Parodi, R. M., Fantetti, K. N. & Fekete, D. M. Non-cell-autonomous planar cell polarity propagation in the auditory sensory epithelium of vertebrates. *Dev. Biol.* **352**, 27–39 (2011).
43. Winter, C. G. et al. Drosophila Rho-associated kinase (Drok) links Frizzled-mediated planar cell polarity signaling to the actin cytoskeleton. *Cell* **105**, 81–91 (2001).
44. Vichas, A. & Zallen, J. A. Translating cell polarity into tissue elongation. *Semin Cell Dev. Biol.* **22**, 858–864 (2011).
45. Dawes-Hoang, R. E. et al. folded gastrulation, cell shape change and the control of myosin localization. *Development* **132**, 4165–4178 (2005).
46. Simoes, SdeM., Mainieri, A. & Zallen, J. A. Rho GTPase and Shroom direct planar polarized actomyosin contractility during convergent extension. *J. Cell Biol.* **204**, 575–589 (2014).
47. Newman-Smith, E., Kourakis, M. J., Reeves, W., Veeman, M. & Smith, W. C. Reciprocal and dynamic polarization of planar cell polarity core components and myosin. *eLife* **4**, e05361 (2015).
48. Shindo, A. & Wallingford, J. B. PCP and septins compartmentalize cortical actomyosin to direct collective cell movement. *Science* **343**, 649–652 (2014).
49. Sai, X., Yonemura, S. & Ladher, R. K. Junctionally restricted RhoA activity is necessary for apical constriction during phase 2 inner ear placode invagination. *Dev. Biol.* **394**, 206–216 (2014).
50. Copley, C. O., Duncan, J. S., Liu, C., Cheng, H. & Deans, M. R. Postnatal refinement of auditory hair cell planar polarity deficits occurs in the absence of Vangl2. *J. Neurosci.* **33**, 14001–14016 (2013).
51. Prakash A., Raman S., Kaushik R., Iyer A. S., Ladher R. K. Mechanical coupling of compartments drives polarity and patterning of mouse auditory epithelium. *bioRxiv*, 2024.2009.2016.613243 (2024).
52. Tilney, L. G., Tilney, M. S., Saunders, J. S. & DeRosier, D. J. Actin filaments, stereocilia, and hair cells of the bird cochlea. III. The development and differentiation of hair cells and stereocilia. *Dev. Biol.* **116**, 100–118 (1986).
53. Amonlirdviman, K. et al. Mathematical modeling of planar cell polarity to understand domineering nonautonomy. *Science* **307**, 423–426 (2005).
54. Luxenburg, C. et al. Wdr1-mediated cell shape dynamics and cortical tension are essential for epidermal planar cell polarity. *Nat. Cell Biol.* **17**, 592–604 (2015).
55. Lawrence, P. A. & Casal, J. Planar cell polarity: two genetic systems use one mechanism to read gradients. *Development* **145**, dev168229 (2018).
56. Strutt, D. Gradients and the specification of planar polarity in the insect cuticle. *Cold Spring Harb. Perspect. Biol.* **1**, a000489 (2009).
57. Mulroy, M. J. & Williams, R. S. Auditory stereocilia in the alligator lizard. *Hear Res.* **25**, 11–21 (1987).
58. Legan, P. K. et al. A targeted deletion in alpha-tectorin reveals that the tectorial membrane is required for the gain and timing of cochlear feedback. *Neuron* **28**, 273–285 (2000).
59. Goodyear, R. J., Lu, X., Deans, M. R. & Richardson, G. P. A tectorin-based matrix and planar cell polarity genes are required for normal collagen-fibril orientation in the developing tectorial membrane. *Development* **144**, 3978–3989 (2017).
60. Mann, Z. F. et al. A gradient of Bmp7 specifies the tonotopic axis in the developing inner ear. *Nat. Commun.* **5**, 3839 (2014).
61. Thiede, B. R. et al. Retinoic acid signalling regulates the development of tonotopically patterned hair cells in the chicken cochlea. *Nat. Commun.* **5**, 3840 (2014).
62. Dabdoub, A. et al. Wnt signaling mediates reorientation of outer hair cell stereociliary bundles in the mammalian cochlea. *Development* **130**, 2375–2384 (2003).
63. Qian, D. et al. Wnt5a functions in planar cell polarity regulation in mice. *Dev. Biol.* **306**, 121–133 (2007).
64. Yamamoto, S. et al. Cthrc1 selectively activates the planar cell polarity pathway of Wnt signaling by stabilizing the Wnt-receptor complex. *Dev. Cell* **15**, 23–36 (2008).
65. Najarro, E. H. et al. Dual regulation of planar polarization by secreted Wnts and Vangl2 in the developing mouse cochlea. *Development* **147**, dev191981 (2020).
66. Landin Malt, A., Hogan, A. K., Smith, C. D., Madani, M. S. & Lu, X. Wnts regulate planar cell polarity via heterotrimeric G protein and PI3K signaling. *J. Cell Biol.* **219**, e201912071 (2020).
67. Navajas Acedo, J. et al. PCP and Wnt pathway components act in parallel during zebrafish mechanosensory hair cell orientation. *Nat. Commun.* **10**, 3993 (2019).
68. Xie, N. et al. Wnt7b acts in concert with Wnt5a to regulate tissue elongation and planar cell polarity via noncanonical Wnt signaling. *Proc. Natl Acad. Sci. USA* **121**, e2405217121 (2024).
69. Sienknecht, U. J. & Fekete, D. M. Mapping of Wnt, frizzled, and Wnt inhibitor gene expression domains in the avian otic primordium. *J. Comp. Neurol.* **517**, 751–764 (2009).
70. Jiang, T., Kindt, K. & Wu, D. K. Transcription factor Emx2 controls stereociliary bundle orientation of sensory hair cells. *eLife* **6**, e23661 (2017).
71. Kindt, K. S. et al. EMX2-GPR156-Galphai reverses hair cell orientation in mechanosensory epithelia. *Nat. Commun.* **12**, 2861 (2021).
72. Lopez-Schier, H. & Hudspeth, A. J. A two-step mechanism underlies the planar polarization of regenerating sensory hair cells. *Proc. Natl Acad. Sci. USA* **103**, 18615–18620 (2006).
73. Singh, N., Prakash, A., Chakravarthy, S. R., Kaushik, R. & Ladher, R. K. In ovo and ex ovo methods to study avian inner ear development. *J. Vis. Exp.: JoVE* e64172 (2022).
74. Singh, N. et al. Mosaic Atoh1 deletion in the chick auditory epithelium reveals a homeostatic mechanism to restore hair cell number. *Dev. Biol.* **516**, 35–46 (2024).
75. Williams, R. M. et al. Genome and epigenome engineering CRISPR toolkit for in vivo modulation of cis-regulatory interactions and gene expression in the chicken embryo. *Development* **145**, dev160333 (2018).
76. Honda, A., Freeman, S. D., Sai, X., Ladher, R. K. & O'Neill, P. From placode to labyrinth: culture of the chicken inner ear. *Methods* **66**, 447–453 (2014).
77. Aigouy, B., Umetsu, D. & Eaton, S. Segmentation and quantitative analysis of epithelial tissues. *Methods Mol. Biol.* **1478**, 227–239 (2016).
78. Schindelin, J. et al. Fiji: an open-source platform for biological-image analysis. *Nat. Methods* **9**, 676–682 (2012).
79. Merkel, M. et al. Triangles bridge the scales: Quantifying cellular contributions to tissue deformation. *Phys. Rev. E* **95**, 032401 (2017).
80. Bolte, S. & Cordelieres, F. P. A guided tour into subcellular colocalization analysis in light microscopy. *J. Microsc.* **224**, 213–232 (2006).
81. Bi, D. P., Lopez, J. H., Schwarz, J. M. & Manning, M. L. A density-independent rigidity transition in biological tissues. *Nat. Phys.* **11**, 1074 (2015).
82. Fletcher, A. G., Osborne, J. M., Maini, P. K. & Gavaghan, D. J. Implementing vertex dynamics models of cell populations in biology within a consistent computational framework. *Prog. Biophys. Mol. Biol.* **113**, 299–326 (2013).

83. Duclut, C., Paijmans, J., Inamdar, M. M., Modes, C. D. & Julicher, F. Nonlinear rheology of cellular networks. *Cells Dev.* **168**, 203746 (2021).
84. Steinberg, M. S. Reconstruction of tissues by dissociated cells. Some morphogenetic tissue movements and the sorting out of embryonic cells may have a common explanation. *Science* **141**, 401–408 (1963).
85. Canty, L., Zarour, E., Kashkooli, L., Francois, P. & Fagotto, F. Sorting at embryonic boundaries requires high heterotypic interfacial tension. *Nat. Commun.* **8**, 157 (2017).
86. Riedel L., Herdeanu B., Mack H., Sevinchan Y., Weninger J. Utopia: A comprehensive and collaborative modeling framework for complex and evolving systems. *J. Open Source Softw.* **5**, 2165 (2020).
87. Sevinchan Y., Herdeanu B., Traub J. dantro: a Python package for handling, transforming, and visualizing hierarchically structured data. *J. Open Source Softw.* **5**, 2316 (2020).
88. Euler L. Elementa doctrinae solidorum. *Novi Commentarii Academiae Scientiarum Petropolitanae* **4**, 109–140 (1758).

Acknowledgements

This work was supported by the Department of Atomic Energy, Government of India, Project Identification No. RTI 4006, and grants from SERB (CRG/2018/001235), TIFR Infosys-Leading Edge Grant, and Royal National Institute for Deaf People (G87) for this research. M.R. acknowledges support from the Simons Foundation (Grant No.\,287975) and DST (India) for a JC Bose Fellowship (JCB/2018/00030). J. W. thanks the University of Geneva Doc mobility programme for financial support. We thank CPDO and TI, Hasserghatta, Bengaluru for providing eggs and Central Imaging and Flow cytometry Facility (CIFF) at NCBS for microscopy imaging. Computations of the vertex model were performed at the University of Geneva's Baobab HPC cluster. A. P. thanks ICTP - ICTS Winter School on Quantitative Systems Biology for providing valuable inputs. We thank Guy Richardson (Sussex Uni, Brighton, UK) and Fumio Matsuzaki (RIKEN BDR, Kobe, Japan) for the gifts of antibodies. The Myo7a antibody developed by Dana J. Orten was obtained from the Developmental Studies Hybridoma Bank, created by the NICHD of the NIH and maintained at The University of Iowa, Department of Biology, Iowa City, IA 52242. We are grateful to the members of our laboratories for their feedback.

Author contributions

R.K.L. and A.P. conceived the project and planned the experiments. A.P. performed, immunostained and imaged the chick BP experiments. A.P. and J.W. analysed the experimental data. S.R. performed volumetric analysis on HC across stages. N.S. performed Atoh1 and Vangl2 knockout experiments. J.W., K.K., and M.R. developed the theory, J.W. implemented the simulations and analysed the simulation results. A.P., J.W., K.K., M.R., and R.K.L. wrote the manuscript.

Competing interests

The authors declare no competing interests.

Additional information

Supplementary information The online version contains supplementary material available at https://doi.org/10.1038/s41467-025-58557-0.

Correspondence and requests for materials should be addressed to Karsten Kruse or Raj K. Ladher.

Peer review information *Nature Communications* thanks the anonymous reviewers for their contribution to the peer review of this work. A peer review file is available.